Summer 2012

Thermal modeling and analysis of polymer electrolyte membrane open cathode fuel cells

Blanca Ollero Loranca

Follow this and additional works at: https://scholarsmine.mst.edu/masters_theses

Part of the Mechanical Engineering Commons

Department:

Recommended Citation

THERMAL MODELING AND ANALYSIS OF POLYMER ELECTROLYTE
MEMBRANE OPEN CATHODE FUEL CELLS

by

BLANCA OLLERO LORANCA

A THESIS

Presented to the Faculty of the Graduate School of the

MISSOURI UNIVERSITY OF SCIENCE AND TECHNOLOGY

In Partial Fulfillment of the Requirements for the Degree

MASTER OF SCIENCE IN MECHANICAL ENGINEERING

2012

Approved by

Robert G. Landers, Advisor
Kelly O. Homan
Umit Koylu

PUBLICATION THESIS OPTION

This thesis has been prepared in the style utilized by the <u>ASME JOURNAL OF FUEL CELLS SCIENCE AND TECHNOLOGY</u>. Pages 7-60 will be submitted for publication in that journal. Appendices A and B have been added for purposes normal to thesis/dissertation writing.

ABSTRACT

In the past decade renewable energies have increasingly become a commodity in everyday life. Because of their high power densities and their application versatility, fuel cells have stood out among other sources of renewable energy. In order to improve this technology as the needs for it increases, thermal modeling is an essential step. Researchers in the past have investigated the effect that temperature has on fuel cells. However, not much work has been done on the thermal dynamics of these devices and no one, to the authors knowledge, has studied the speed of response in thermal changes as a function of stack size, current demand or mass flow rate of air.

This research presents a one-dimensional lumped model for an open cathode polymer electrolyte fuel cell. This study analyzes the contribution of all the heat sources traditionally involved in the thermal study of fuel cells, and determines simplifications that have not been identified previously in the literature. Moreover, this work presents an analysis of open cathode fuel cells by comparing the fuel cell stack to a heat exchanger. This analogy provides researchers with a tool to evaluate heat dissipation in air breathing fuel cells without having to develop a complicated electrochemical model that would have to account for mass transport phenomena. Finally, this analysis studies both the steady state and transient thermal distribution in the fuel cell stack and how this distribution is affected by stack size, operation current and mass flow rate of air flowing though the cathode/cooling channels.

ACKNOWLEDGMENTS

First of all I would like to thank my advisor, Dr. Robert Landers, for his patience and guidance. He provided me with funding through a graduate teaching assistantship and includED me in a project with the National Science Foundation (EEC−1004839). I would also like to thank my committee members, Dr. Kelly Homan and Dr. Umit Koylu, for taking the time out of their schedules to review my work and provide feedback. Thank you Dr. Homan for helping out with the thermal modeling. Also, thank you Dr. Koylu for teaching me all the basics of fuel cell and giving me a starting point in my research.

I would like to thank my family, for their encouragement, understanding and support; I know it is hard to be far apart but without you I would not be where I am or who I am today. Additionally, I would like to thank my wonderful fiancé for bringing me up when I am down, opening a window every time I reach a dead end.

TABLE OF CONTENTS

LIST OF ILLUSTRATIONS

LIST OF TABLES

1. INTRODUCTION

1.1 MOTIVATION

For the past 200 years industry has heavily relied on the use of fossil fuels. It was not until the 1970s that the aftermath of this excessive use of fossil fuels started to concern the general public. Ever since, the scientific community has been researching alternative ways to provide energy while reducing or completely eliminating greenhouse gas (GHG) emissions. In 1997, the United Nations came to an agreement known as the Kyoto Protocol. The most outstanding characteristic of the Kyoto protocol is that it sets constraints to 37 industrialized countries and the European community for reducing GHG emissions to an average of 5% of 1990 levels over the 5 year-period 2008-2012 [1]. The protocol entered into force in 2001. These imposed restrictions have been the main driving force behind the boom of research in renewable energies such as solar, wind, geothermal, nuclear, batteries, fuel cells, etc. Due to the higher power density, scaling, economical affordability, safety measures and resource availability that fuel cells offer in comparison to other renewable energy options, this research concentrates on fuel cells. More specifically, this research focuses on the thermal modeling of fuel cell which is a key determining factor for their durability and efficiency.

1.2 FUEL CELL OPERATION

Fuel cells are electrochemical devices that convert the chemical energy of a reaction directly into electrical energy. The hydrogen combustion reaction is split into two electrochemical reactions

$$H_2 \rightleftharpoons 2H^+ + 2e^- \tag{1}$$

$$\frac{1}{2}O_2 + 2H^+ + 2e^- \rightleftharpoons H_2O \tag{2}$$

When these two reactions are physically separated, the electrons from the hydrogen can be conducted to a load through an electric circuit before completing the reaction. The electrodes (anode and cathode) in which the reactions take place are

separated by an electrolyte that allows ions, but not electrons to flow through. Figure 1.1 shows the schematic of the basic unit of a fuel cell.
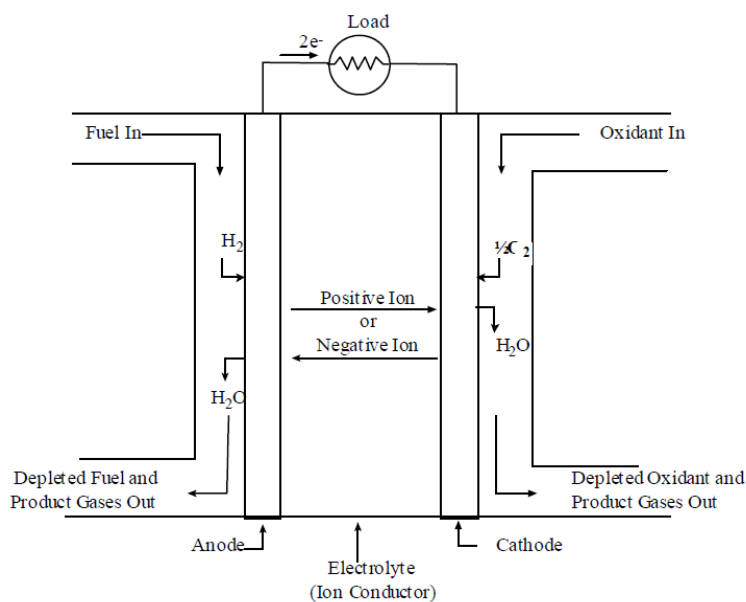
Figure 1.1. Schematic of an single cell fuel cell [2].

By stacking multiple units together, fuel cells of different power capabilities can be configured. As Figure 1.1 shows, in a typical fuel cell fuel (generally hydrogen) and oxidant are continuously fed into the anode and cathode, respectively. For this reason, fuel cells are often compared to combustion engines. However, since fuel cells convert chemical energy into electrical energy, they are more efficient than combustion engines. Also, fuel cells have no moving parts, this making them a more reliable and longer lasting system than a combustion engine. Moreover, fuel cells do not emit undesirable gases, such as NO_x, SO_x, or particulates. Also, due to their components and characteristics, fuel cells can also be compared to batteries. However, while fuel cell's capacity is determined by the amount of fuel supplied, batteries act like a reservoir only

containing as much energy as chemical reactant can be stored in it. After the battery is discharged, it has to be connected to another power supply in order for it to be useful again. Fuel cells have a highly scalable design, which makes them suitable as electrical generators in large power plants or buildings. They are also widely used for mobile applications such as in the automotive industry, laptops or smaller electronics such as cell phones.

There are multiple types of fuel cells that are characterized by the combination of types of fuel and oxidant they utilize, fuel reforming capabilities, the type of electrolyte, the operating temperature, whether the reactants are fed to the cell by internal or external manifolds, etc. However, the most common fuel cell classification is by type of electrolyte: polymer electrolyte membrane fuel cell (PEMFC), alkaline fuel cell (AFC), phosphoric acid fuel cell (PAFC), molten carbonate fuel cell (MCFC), and solid oxide fuel cell (SOFC) [2]. The operating temperatures of these different types of fuel cells range from ~80°C (PEMFC) to 1000°C (SOFC). The fuel cell operating temperature is a key factor for the operating life of the fuel cell. The fuel cell temperature will affect the degradation of the electrodes and electrolyte, as well as the rate at which the chemical reaction will be converted to electrical power. This thesis focuses on the importance of the thermal modeling of these fuel cell systems.

The PEMFCs are the most commonly used fuel cells for every-day-use applications because of their low operating temperature. For that reason they have also been a main research focus for years. The PEMFCs use a thin polymer membrane as electrolyte to conduct ions. Moreover, PEMFCs have to be fed pure hydrogen and will use either pure oxygen or air as the oxidant. The material used for the membrane in the majority of PEMFCs is Nafion®. In order to promote the transfer of electrons, this membrane has to be properly hydrated. Nafion® membranes are characterized by having a polytetrafluoroethylene structure bonded to sulfonic acid $\left(SO_3^-H^+\right)$ chains that provide charge sites for proton transport [3]. When sufficient water exists in the membrane, ionic conduction in the membrane behaves in a similar way to that in a liquid electrolyte. Water in the fuel cell is constantly being created by the electro-chemical reaction. On the other hand, at high temperatures water will also be constantly evaporated. Flooding and dehydration will limit the longevity of the membrane and the fuel cell. Therefore, water

management is another key factor for the proper functionality of the cell. As it can be seen, water and temperature management are very tightly linked together. Both factors not only affect the durability of the fuel cell, but also the reaction rate, which determines the fuel cell efficiency.

2. LITERATURE REVIEW

In the 1990s several one dimensional models were published [4-7], but these models do not model any cooling mechanism. Amphlett et al. [5] developed a dynamic cell stack model; however, like [4, 6, 7], the temperature distribution through the stack was not studied. In 2000, R.F. Mann et al. [8] and N. Djilali et al. [9] developed more complicated one dimensional fuel cell models. These models described only steady-state temperature characteristics. Later,Yang et al. [10] presented a complete three dimensional CFD thermal model and experimental validation of their results. However, the experimental validation provided does not include the temperature distribution throughout the stack. Instead, the validation is only done through the fuel cell polarization curve at different operating temperatures. Later, more detailed models that incorporated more layers in the fuel cell were published [11-13]. Xue et al. [12] provided experimental validation; however, the empirical data only provided insight of the reactant flow rates, and membrane current and voltage. During this time [11 and 13] major advances were achieved in the study of water throughout the membrane and how it was affected by temperature changes. As it can be seen, the literature regarding fuel cell modeling before 2008 [14-20] does not show any major steps in the study of temperature effects or management within a fuel cell stack References [14-19] validate focus their thermal modeling through observations of the polarization curve. However, no real insight of the temperature distribution within the stack was obtained. Spiegel [20] developed an FEA model that divided the fuel cell into layers, each layer representing a finite element. The analysis then proceeded through an energy balance. However, the analysis does not include thermal contact resistance between the materials and combines the energy balance between layers and their heat transfer through conduction. Spiegel [20] only validated her results based off of the data obtained through the polarization curve. Gao and Blunier [21] developed a thermal model, similar to [20], and studied the temperature distribution in the fuel cell stack and its evolution in time for different current inputs. However, neither of these models included thermal contact resistances, which is crucial for correct thermal modeling.

Fuel cell research has led to a new generation of PEM fuel cells which incorporate an air cooling system to the oxidant feeding channels. This new configuration presents noticeable advantages in the fuel cell industry such as the elimination of an independent supply for pure oxygen making fuel cells more suitable for portable applications. Rajani et al. [22] developed a two-dimensional steady-state non-isothermal model for these types of fuel cells. Sasmito et al. [23] developed a two-phase mathematical model that concentrated on the flow-field of forced air through the stack cooling channels and its effect on the stack performance. O'Hayre et al. [24] studied a one-dimensional, non-isothermal model that combined heat and mass transport in a air-breathing natural convection PEM fuel cell. Momer et al. [25] studied the effect of temperature on humidity for air-breathing fuel cells. Lister et al. [26] developed a three-dimensional thermal model for microstructured air-breathing fuel cells using finite difference methods.

2.1 RESEARCH CONTRIBUTION

The model presented in this research is a detailed thermal model of a PEM fuel cell stack based on first principles that uses thermal contact resistances to calculate the heat transferred between the different fuel cell layers. The analysis of this model will answer some questions not yet addressed in the literature. This work clearly establishes the relationship between the different contributions to the heat generation in the fuel cell to the current drawn. Also, the model mathematically analyzes all elements traditionally involved in the energy balance of the fuel cell and reveals some simplifications that have not examined before. The work presented in this thesis also offers a new perspective to the analysis of open cathode fuel cells by comparing the stack to a heat exchanger. This comparison provides researchers and designers with a tool to quickly evaluate heat dissipation in the fuel cell stack. The analysis carried out in this work studies in detail the speed of response of the system's temperature to different inputs. This analysis will help in the design of controllers for these fuel cell systems by providing a better understanding of their dynamics to the scientific community.

PAPER

I. Thermal Modeling and Analysis of Polymer Electrolyte Membrane Open Cathode Fuel Cells

Blanca Ollero-Loranca

Missouri University of Science and Technology

Rolla, Missouri

both5@mst.edu

Dr. Robert Landers

Missouri University of Science and Technology

Rolla, Missouri

landersr@mst.edu

Abstract

In the past decade renewable energies have increasingly become a commodity in everyday life. Because of their high power densities and their application versatility, fuel cells have stood out among other sources of renewable energy. In order to improve this technology as the needs for it increases, accurate thermal modeling is essential. Researchers in the past have investigated the effect that temperature has on fuel cell performance. However, not much work has been done on the analysis of the thermal dynamics of these devices and no one, to the authors' knowledge, has studied the speed of response in thermal changes as a function of stack size, current demand and air mass flow rate.

This paper presents a one-dimensional lumped model for an open cathode polymer electrolyte fuel cell. This study analyzes the contribution of all of the heat sources traditionally involved in the thermal study of fuel cells, and determines simplifications that have not been identified previously in the literature. Moreover, this work presents an analysis of open cathode fuel cells by comparing the fuel cell stack to a heat exchanger. This analogy provides researchers with a tool to evaluate heat dissipation in air breathing fuel cells without having to develop a complicated electrochemical model that would have to account for mass transport phenomena. Finally, this analysis studies both the steady state and transient thermal distribution in the

fuel cell stack and how this distribution is affected by stack size, operation current and mass flow rate of air flowing though the cathode/cooling channels.

1 Introduction

In 1997, the United Nations came to an agreement known as the Kyoto Protocol in which the participating countries committed to reduce their greenhouse gas emissions by 5% by 2012. These imposed restrictions have been the main driving force behind the boom of research in renewable energies such as solar, wind, geothermal, nuclear, batteries, fuel cells, etc. Due to higher power density, scaling, resource availability and the non-existence of toxic biproducts that fuel cells offer in comparison to other renewable energy options, fuel cells have received substantial focus in the literature. The research conducted in this paper focuses on the thermal modeling of fuel cells, which is a key determining factor for their durability and efficiency.

Fuel cells are electrochemical devices that convert the chemical energy of a reaction directly into electrical energy. The hydrogen combustion reaction is split into two electrochemical reactions

$$H_2 \rightleftharpoons 2H^+ + 2e^- \tag{1}$$

$$\frac{1}{2}O_2 + 2H^+ + 2e^- \rightleftharpoons H_2O \tag{2}$$

When these two reactions are physically separated, the electrons from the hydrogen can be conducted to a load through an electric circuit before completing the reaction. The electrodes (anode and cathode) in which the reactions take place are separated by an electrolyte that allows ions, but not electrons to flow through.

There are multiple types of fuel cells that are characterized by the combination of the types of fuel and oxidant they utilize, fuel reforming capabilities, type of electrolyte, operating temperature, whether the reactants are fed to the cell by internal or external manifolds, etc. However, this paper concentrates on Polymer Electrolyte Membrane Fuel Cells (PEMFC) as they are very common due to their low operating temperature (~80°C). The fuel cell operating temperature is a key factor for the operating life of the fuel cell.

The fuel cell temperature will affect the degradation of the electrodes and electrolyte, as well as the rate at which the chemical reaction will be converted to electrical power. This paper focuses on the thermal modeling of PEM fuel cells.

The PEMFCs use a thin polymer membrane as electrolyte to conduct ions. Moreover, PEMFCs have to be fed pure hydrogen and will use either pure oxygen or air as the oxidant. The material used for the membrane in the majority of PEMFCs is Nafion®. In order to promote the transfer of electrons, this membrane has to be properly hydrated. Water in the fuel cell is constantly being created by the electro-chemical reaction. On the other hand, at high temperatures water will be constantly evaporated. Flooding and dehydration will limit the longevity of the membrane and, thus, the fuel cell. Therefore, water management is another key factor for proper fuel cell functionality. As it can be seen, water and temperature management are very tightly linked together. Both factors not only affect fuel cell durability, but also the reaction rate, which determines fuel cell efficiency.

In order to control the fuel cell temperature to obtain optimal water activity and overall efficiency, modeling is the first step. Many fuel cell thermal models have been developed. Most of these models only focus on the static behavior of the fuel cell temperature or the dynamic behavior of the membrane. The fuel cell thermal models developed so far incorporate lumped energy equations. However, many of these models do not provide the temperature distribution throughout the stack. Instead, many of the models in the literature show the effects of the operating temperature on the stack performance.

In the 1990s several one dimensional models were published [1-4], but these models do not include a cooling mechanism. Amphlett et al. [2] developed a dynamic cell stack model; however, similar to [1, 3, 4], the temperature distribution through the stack was not studied. In 2000, Mann et al. [5] and Djilali et al. [6] developed more complicated one dimensional fuel cell models that only described steady-state temperature characteristics. Later, Yang et al. [7] presented a complete three dimensional CFD thermal model and experimental validation of their results. However, the experimental validation provided does not include the temperature distribution throughout the stack. Instead, the validation is only done through the fuel cell

polarization curve at different operating temperatures. Later, more detailed fuel cell systems thermal models that include more components in the fuel cell stack were developed [8-10]. Xue et al. [9] provided experimental validation; however, the empirical data only provided insight of the reactant flow rates, and membrane current and voltage. During this time major advances were achieved in the study of water concentration in the membrane and how it was affected by temperature changes [8, 10]. The work in [11-16] only validate their thermal fuel cell models through observations of the polarization curve. However, no insight of the temperature distribution within the stack was obtained. Spiegel [17] developed an FEA model that divided the fuel cell into layers, each layer representing an element. The analysis then proceeded through an energy balance. However, the analysis does not include thermal contact resistance between the materials and combines the energy balance between layers and their heat transfer through conduction. Spiegel [17] only validated her results based off of the data obtained through the polarization curve. Gao and Blunier [18] developed a thermal model, similar to [17], and studied the temperature distribution in the fuel cell stack and its evolution in time for different current inputs. However, neither of these models included thermal contact resistances, which is crucial for correct thermal modeling.

Fuel cell research has led to a new generation of PEM fuel cells which incorporate an air cooling system to the oxidant feeding channels. This new configuration presents noticeable advantages in the fuel cell industry such as the elimination of an independent supply for pure oxygen making fuel cells more suitable for portable applications. Rajani et al. [19] developed a two-dimensional steady-state non-isothermal model for these types of fuel cells. Sasmito et al. [20] developed a two-phase mathematical model that concentrated on the flow-field of forced air through the stack cooling channels and its effect on the stack performance. O'Hayre et al. [21] studied a one-dimensional, non-isothermal model that combined heat and mass transport in a air-breathing natural convection PEM fuel cell. Momer et al. [22] studied the effect of temperature on humidity for air-breathing fuel cells. Lister et al. [23] developed a three-dimensional thermal model for microstructured air-breathing fuel cells using finite difference methods.

The model presented in this research is a detailed thermal model of a PEM fuel cell stack based on first principles that uses thermal contact resistances to calculate the heat transferred between the different fuel cell layers. The analysis of this model will answer some questions not yet addressed in the literature. This work clearly establishes the relationship between the different contributions to the heat generation in the fuel cell to the current drawn. Also, the model mathematically analyzes all elements traditionally involved in the energy balance of the fuel cell and reveals some simplifications that have not been previously examined before. The work presented in this paper also offers a new perspective to the analysis of open cathode fuel cells by comparing the stack to a heat exchanger. This comparison provides researchers and designers with a tool to quickly evaluate heat dissipation in the fuel cell stack. The analysis conducted in this work studies in detail the speed of response of the system's temperature to different inputs, such as air mass flow rate and current demand. This analysis will help in the design of controllers for these fuel cell systems by providing a better understanding of their dynamics.

2 Single Cell Model

The schematic of a single cell fuel cell is shown in Figure 1. The fuel cell temperature is modeled by coupling the equations that describe the five layers shown in Figure 1: two end plates, two bipolar plates and one Membrane Electrode Assembly (MEA).
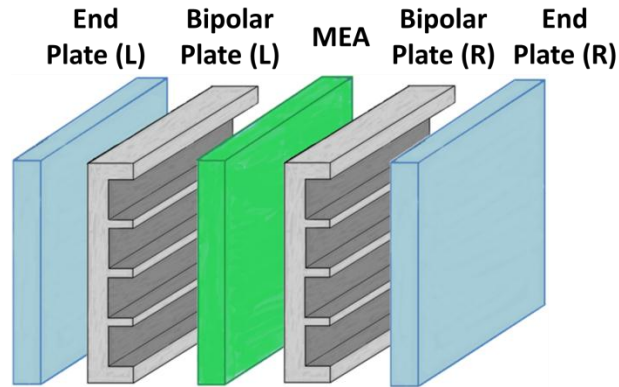
Fig. 1. Single cell fuel cell schematic.

The heat balance for the single cell fuel cell is displayed in Figure 2. Five differential equations governing this system are derived by performing an energy balance of each layer. Two algebraic equations describing the heat dissipated by the fluid are derived by performing a fluid energy balance.
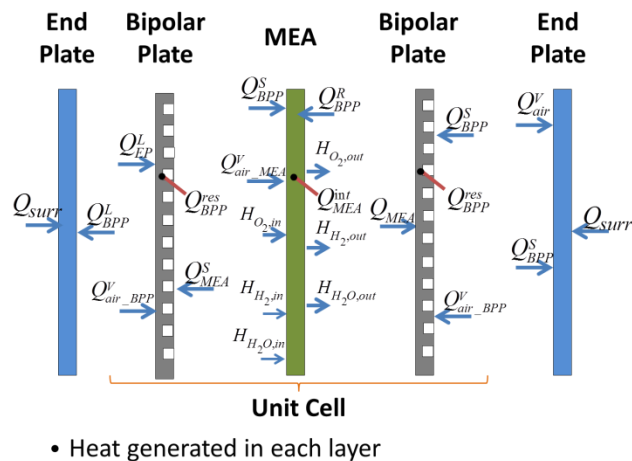
Fig. 2. Single cell heat balance.

2.1 Left End Plate. The differential equation describing the heat transfer

dynamics of the left end plate is

$$\frac{dT_{EP}^{L}(t)}{dt} = \frac{Q_{surr}^{L}(t) + Q_{BPP}^{L}(t)}{\tau_{EP}} \tag{3}$$

where T_{EP}^{L} is the left end plate temperature (K), Q_{surr} is the convective heat coming from

the fuel cell surroundings (W), $Q_{EP,BPP}$ is the conductive heat transferred from the left

bipolar plate to the end plate (W) and τ_{EP} is the end plate thermal mass (J/K). The terms

in equation (3) are

$$Q_{surr}^{L}(t) = h_{surr} A_{EP} \left(T_0 - T_{EP}^{L}(t) \right) \tag{4}$$

$$Q_{EP,BPP}(t) = \frac{A_{BPP}^{L}}{R_{EP,BPP}^{"}} \left(T_{BPP}^{L}(t) - T_{EP}^{L}(t) \right) \tag{5}$$

$$\tau_{EP} = A_{EP} l_{EP} \rho_{EP} c_{EP} \tag{6}$$

where h_{surr} is the convective heat transfer coefficient from the fuel cell's surroundings

(W/m²K), A_{EP} is the end plate area (m²), A_{BPP}^{L} is the bipolar plate left face area (m²),

$R_{EP,BPP}^{"}$ is the thermal contact resistance between the end plate and the bipolar plate

(m²·K/W), l_{EP} is the end plate thickness (m), ρ_{EP} is the end plate density (kg/m³), c_{EP} is

the end plate specific heat (J/g·K), T_0 is the environmental temperature (K), T_{EP}^{L} is the left

end plate temperature (K) and T_{BPP}^{L} is the left bipolar plate temperature (K).

2.2 Left Bipolar Plate. The left face of the bipolar plate is a flat surface.
However, the right face of the bipolar plate has channels embedded in it. For this reason,
both the conduction from the layer to the right of the bipolar plate and the convection
from the air flowing through the channels will have to be taken into account. Two
different areas are considered

$$A_{BPP}^{S} = \left(a^{S} \left(N_{chan} - 1 \right) + 2b^{S} \right) w_{BPP} \tag{7}$$

$$A_{BPP}^V = \left(a^V w_{BPP} + 2l_{chan} w_{BPP}\right) N_{chan} \tag{8}$$

where A_{BPP}^S is the area of the solid part of the right face of the bipolar plate (m^2), A_{BPP}^V is the area of the bipolar plate in contact with the air flowing through the channels (m^2) and N_{chan} is the number of channels. The other variables are illustrated in Figure 3.
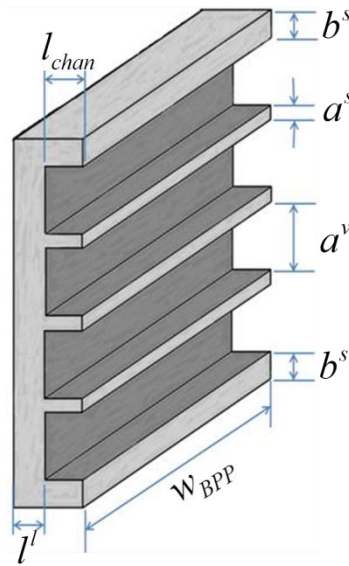
Fig. 3. Bipolar plate dimensions.

The heat generated by the bipolar plate is only caused by Joulean heating. According to Joule's Law, the energy generated by any electrical device is

$$Q = i^2 R \tag{9}$$

where Q is the energy generated (W), R is the electrical resistance (Ω) and i is the current (A). The energy that is not converted to electrical energy will be lost as heat energy. The differential equation describing the heat transfer dynamics of the left bipolar plate is

$$\frac{dT_{BPP}^{L}(t)}{dt} = \frac{-Q_{EP,BPP}(t) + Q_{BPP,MEA}^{S}(t) + Q_{air\_BPP}^{L}(t) + Q_{BPP}^{res}}{\tau_{BPP}} \tag{10}$$

where T_{BPP}^{L} is the left bipolar plate temperature (K), Q_{EP}^{L} is the heat transferred by conduction from the left end plate to the left bipolar plate (W), $Q_{BPP,MEA}^{s}$ is the heat transferred by conduction from the MEA to the solid part of left bipolar plate in contact with the MEA (W), $Q_{air\_BPP}^{L}$ is the convective heat dissipated by the air in the channels of left bipolar plate (W), Q_{BPP}^{res} is the heat generated by the current flowing through the bipolar plate (W), which is solely caused by Joulean heating, and τ_{BPP} is the bipolar plate thermal mass (J/K). The terms in equation (10) are

$$Q_{BPP,MEA}^{S}(t) = \frac{A_{BPP}^{S}}{R_{MEA,BPP}^{"}}\left(T_{MEA}(t) - T_{BPP}^{L}(t)\right) \tag{11}$$

$$Q_{air\_BPP}^{L}(t) = h_{chan}A_{BPP}^{V}\left(T_{air}^{L}(t) - T_{BPP}^{L}(t)\right) \tag{12}$$

$$Q_{BPP}^{res}(i) = i^{2}\frac{\rho_{BPP}^{res}l_{BPP}}{A_{BPP}} \tag{13}$$

$$\tau_{BPP} = \rho_{BPP}A_{BPP}^{L}l_{BPP}c_{BPP} \tag{14}$$

where $R_{MEA,BPP}^{"}$ is the thermal contact resistance between the MEA and the bipolar plate (m^2·K/W), l_{BPP} is the bipolar plate thickness (m), l_{MEA} is the MEA thickness (m), h_{chan} is the convective heat transfer coefficient in the channels (W/m^{2}K), ρ_{BPP} is the bipolar plate density (kg/m^3), c_{BPP} is the bipolar plate specific heat (J/g·K), i is the current through the stack (A), ρ_{BPP}^{res} is the bipolar plate material electrical resistance (Ω·m), T_{MEA} is the MEA temperature (K) and T_{air}^{L} is the air temperature in the channels of the left bipolar plate (K).

The convective heat transfer coefficient is dependent on the flow regime, which consists of the flow development and the channel geometry. The effective diameter (i.e., hydraulic diameter) of the square channel (m) is

$$D_H = \frac{2a^V w^V}{a^V + w^V} \tag{15}$$

where w^V is the channel width (m) and a^V is the channel height (m) illustrated in Figure 3. The Reynolds number is

$$\mathrm{Re}_D = \frac{4\dot{m}_{air}}{\pi D_H \mu} \tag{16}$$

where μ is the fluid viscosity (kg/m·s). Turbulent flow occurs if $\mathrm{Re} \geq 2300$ [24]. If the flow is turbulent and $L/D_H \geq 10$, the flow will be fully developed. Also, if the flow is laminar and $L/D_H \geq 5\times10^{-2}\mathrm{RePr}$, where Pr is the Prandtl number, the flow will be fully developed as well. The Nusselt number is

$$\mathrm{Nu}_D = \frac{hD_H}{k} = f\left(\mathrm{Re}_D, \mathrm{Pr}\right) \tag{17}$$

where k is the fluid conduction heat transfer coefficient (W/m·K). In turbulent fully developed flow, when $0.5 \leq \mathrm{Pr} \leq 2000$ and $3000 \leq \mathrm{Re}_D \leq 5\times10^6$, the Nusselt number is [24]

$$\mathrm{Nu}_D = \frac{(f/8)(\mathrm{Re}_D - 1000)\mathrm{Pr}}{1 + 12.7(f/8)^{1/2}\left(\mathrm{Pr}^{2/3} - 1\right)} \tag{18}$$

where f is the Moody friction factor [24]. The fuel cell air channels can be approximated by correlations that accurately approximate the smooth surface condition. Such relations are

$$\begin{aligned} f &= 0.316\,\mathrm{Re}_D^{-1/4} && \text{for } \mathrm{Re}_D \leq 2\times10^4 \\ f &= 0.184\,\mathrm{Re}_D^{-1/5} && \text{for } \mathrm{Re}_D > 2\times10^4 \end{aligned} \tag{19}$$

In fully developed laminar flow, with the fuel cell channel geometries considered in this study, $\mathrm{Nu} \approx 3.39$. However, if the conditions determine that the flow is developing throughout the channel, the Nusselt number is then [24]

$$\mathrm{Nu}_D = 3.39 + \frac{0.0668(D_H/w_{BPP})\mathrm{Re}_D\,\mathrm{Pr}}{1 + 0.04\left[(D_H/w_{BPP})\mathrm{Re}_D\,\mathrm{Pr}\right]^{2/3}} \tag{20}$$

2.3 Membrane Electrode Assembly. The irreversible reaction heat and entropic heat in the cathode catalyst layer are the major contributors to heat generation in the PEM fuel cell, accounting for roughly 80 to 90% of the total waste heat released [28]. The differential equation describing the heat transfer dynamics of the MEA is

$$\frac{dT_{MEA}(t)}{dt} = \frac{Q^R_{BPP,MEA}(t) - Q^S_{BPP,MEA}(t) + Q^V_{air\_MEA}(t) + \Delta H + Q^{int}_{MEA}(t)}{\tau_{MEA}} \tag{21}$$

where, $Q^R_{BPP,MEA}$ is the heat transferred from the left face of the right bipolar plate to the MEA by conduction (W), $Q^V_{air\_MEA}$ is the heat dissipated from the MEA by the air in the channels of the left bipolar plate by convection (W), ΔH is the change of enthalpy of the species in the MEA (W), Q^{int}_{MEA} is the internal heat generated in the MEA (W) and τ_{MEA} is the MEA thermal mass (J/K). The terms in equation (21) are

$$Q^R_{BPP,MEA}(t) = \frac{A^L_{BPP}}{R^{"}_{MEA,BPP}}\left(T^R_{BPP}(t) - T_{MEA}(t)\right) \tag{22}$$

$$Q^V_{air\_MEA}(t) = h_{chan}A^V_{MEA}\left(T^L_{air}(t) - T_{MEA}(t)\right) \tag{23}$$

$$\Delta H(t) = \Delta H_{H_2O}(t) + \Delta H_{H_2}(t) + \Delta H_{O_2}(t) \tag{24}$$

$$\Delta H_{H_2O}(t) = J^{net}_{H_2O}A_{MEA}MW_{H_2O}\left(T_A(t) - T_C(t)\right) \tag{25}$$

$$\Delta H_{H_2}(t) = \dot{m}_{H_2,c}c_{H_2}\left(T_{H_2,out}(t) - T_{H_2,in}\right) \tag{26}$$

$$\Delta H_{O_2}(t) = \dot{m}_{O_2,c}c_{O_2}\left(T_{O_2,out}(t) - T_{O_2,in}\right) \tag{27}$$

$$\tau_{MEA} = \rho_{MEA}A_{MEA}l_{MEA}c_{MEA} \tag{28}$$

where ΔH_{H_2O} is the change of enthalpy of the water present in the MEA (W), ΔH_{H_2} is the change of enthalpy of the hydrogen present in the MEA (W), ΔH_{O_2} is the change of enthalpy of the oxygen present in the MEA (W), MW_{H_2O} is the molecular weight of water (18 g/mol), T_A is the anode temperature (K), which is assumed to be the same as T^R_{BPP}, T_C

is the cathode temperature (K), which is assumed to be the same as T_{BPP}^L, $T_{H_2,out}$ is the temperature of the hydrogen at the stack outlet (K), which is assumed to be the same as T_{MEA}, $T_{H_2,in}$ is the temperature of the hydrogen at the stack inlet (K), which is assumed to be the same as T_{BPP}^R, $T_{O_2,out}$ is the temperature of the oxygen at the stack outlet (K), which is assumed to be the same as T_{MEA}, $T_{O_2,in}$ is the temperature of the oxygen at the stack inlet (K), which is assumed to be the same as T_{BPP}^R, A_{MEA} is the MEA area (m²), ρ_{MEA} is the MEA density (kg/m³), c_{MEA} is the MEA specific heat (J/g·K), c_{H_2O} is the specific heat of the water present in the MEA (J/g·K), c_{H_2} is the specific heat of hydrogen (J/g·K), c_{O_2} is the specific heat of oxygen (J/g·K), A_{MEA}^V is the total area of the MEA in contact with the air flowing through the channel (m²), T_{BPP}^R is the right bipolar plate temperature (K) and $\dot{m}_{H_2O}$ is the mass flow rate of water in the MEA (g/s).

Hydrogen and oxygen coming from the anode and cathode, given by flow rates $\dot{m}_{H_2}$ and $\dot{m}_{O_2}$, respectively, are consumed in the MEA while water is being generated. The consumption mass flow rate of the species (g/s) is

$$\dot{m}_c = \frac{i}{n^e F} MW \qquad (29)$$

where *MW* is the molecular weight of the species being consumed (g/mol), i.e., hydrogen or oxygen.
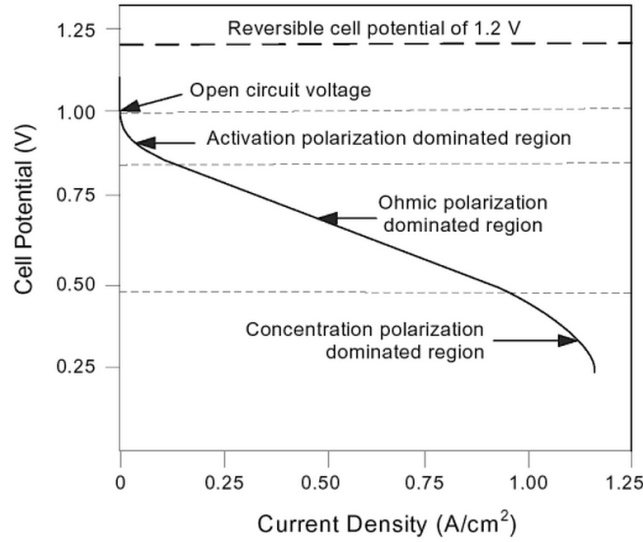
Fig. 4. Example of a PEM fuel cell polarization curve [25].

In fuel cells, multiple losses occur during operation that affect the heat generation in the MEA. As Figure 4 illustrates, such losses can be depicted in a polarization curve and categorized as activation losses, ohmic losses and concentration losses. The total fuel cell operating voltage is

$$E_{total}(t) = E_{thermo}(t) - \eta_{act}(j) - \eta_{ohmic}(j) - \eta_{conc}(j) \qquad (30)$$

where E_{total} is the total fuel cell operating voltage (V), E_{thermo} is the ideal thermodynamic voltage at the operating conditions, i.e., operating temperature and pressure, (V), η_{act} is the activation voltage loss (V), η_{ohmic} is the ohmic voltage loss (V), η_{conc} is the concentration voltage loss (V) and j is the fuel cell current density (A/cm^2). These terms are modeled, respectively, by [29]

$$E_{thermo} = E^0 + \frac{\Delta s}{n_e F}(T - T_0) - \frac{RT}{n_e F} \ln\left(\frac{\Pi a_P^{v_i}}{\Pi a_R^{v_i}}\right) \qquad (31)$$

$$\eta_{act} = a + b\log(j) \qquad (32)$$

$$\eta_{ohmic} = j\left(ASR_{ohmic}\right) \tag{33}$$

$$\eta_{conc} = c\ln\left(\frac{j_L}{j_L - j}\right) \tag{34}$$

where E^0 is the open circuit potential voltage (1.229 V), n_e is the number of electrons involved in the reaction, F is Faraday's constant, Δs is the entropy change of the reaction taking place in the fuel cell, T is the operation temperature (K), R is the ideal gas constant, $a_P^{v_i}$ and $a_R^{v_i}$ are, respectively, the activities of each species in the products and the reactants (atm), a and b are parameters obtained from Taffel kinetics, ASR_{ohmic} is the area normalized fuel cell resistance ($\Omega\cdot cm^2$), c is a constant that defines the concentration losses and j_L is the fuel cell limiting current density (A/cm^2). However, E_{total} can also be modeled as [27]

$$E_{total}(t) = E_{thermo}(t) - A\ln(j) - jR - m\,e^{nj} \tag{35}$$

Equation (35) is a semiempirical model whose parameters are obtained from the nominal fuel cell polarization curve.

Internal heat generation in the membrane is caused by the entropic heat of reactions (irreversible heat of electrochemical reactions) responsible for concentration and activation overpotentials, as well as Joulean heating. The heat generated in the MEA is

$$Q_{MEA}^{int}(t) = i\left\{\left[\frac{\Delta s}{n_e F} - \frac{R}{n_e F}\ln\left(\frac{\Pi a_P^{v_i}}{\Pi a_R^{v_i}}\right)\right]T_{MEA}(t) + \eta_{act}(j) + \eta_{conc}(j) + \eta_{ohmic}(j)\right\} \tag{36}$$

Comparing equation (36) to the power output of a fuel cell operating at voltage E_{total}, obtained from equation (31), and current i, it is observed that a PEM fuel cell produces nearly a similar amount of waste heat as it does electric output power, rendering an energy conversion efficiency of roughly 50% [28].

It is important to note that ASR_{ohmic} is highly dependent on the water content in the membrane and the membrane thickness. One of the most commonly used polymer electrolytes in fuel cells is Nafion®. It has been well established in the literature that

proton conductivity in Nafion® increases linearly with increasing water content and exponentially with increasing temperature [29]

$$\sigma\left(T_{MEA}(t), \lambda\right) = \sigma_{303K}(\lambda) \exp\left[1268\left(\frac{1}{303} - \frac{1}{T_{MEA}(t)}\right)\right] \tag{37}$$

$$\sigma_{303K}(\lambda) = 5.193 \times 10^{-3}\lambda - 3.26 \times 10^{-3} \tag{38}$$

where σ is the membrane conductivity (S/cm) and λ is the water content in the membrane (cm^2/s). Now, ASR_{ohmic} is

$$ASR_{ohmic} = \int_{0}^{\Delta x_{MEA}} \frac{dx}{\sigma\left[\lambda(x)\right]} \tag{39}$$

Nafion® membranes used in the fabrication of polymer electrolyte membrane fuel cells have sulfonic acid $\left(SO_3^-H^+\right)$ chains that provide charge sites for proton transport [29]. When sufficient water exists in the membrane, ionic conduction occurring in it is similar to that in liquid electrolytes. For this reason it is imperative to always keep the membrane fully hydrated.

The ratio of the number of water molecules to the number of charged $\left(SO_3^-H^+\right)$ sites in the Nafion® membrane is the water content. Springer et al. [30] developed the model of variable membrane hydration. Their experimental results suggested that λ can vary from almost 0 (for completely dehydrated Nafion®) to 22 (for full saturation at 100^oC) and 16.8 when the membrane is fully saturated at 80^oC. For the purpose of the studies conducted this paper, the MEA is considered to always be fully hydrated; therefore, $\lambda = 22$. For values of water content greater than 4 cm^2/s, water diffusivity is [29]

$$D_\lambda = \exp\left[2416\left(\frac{1}{303} - \frac{1}{T}\right)\right] \times \left(2.563 - 0.33\lambda + 2.64 \times 10^{-2}\lambda^2 - 6.71 \times 10^{-4}\lambda^3\right) \times 10^{-6} \tag{40}$$

In order to obtain the water mass flow rate within the membrane, the water content can be converted to water concentration in Nafion®

$$C_{H_2O} = \lambda \frac{\rho_{dry}}{M_m} \tag{41}$$

where C_{H_2O} is the water concentration in Nafion® (mol/m^3), ρ_{dry} is the membrane dry density (~1970 kg/m^3) and M_m is Nafion® dry density (~1.1 kg/mol).

The number of water molecules dragged by each proton in the membrane is called the electro-osmotic drag coefficient, n_{drag}. This coefficient determines the water movement within the membrane and varies linearly with the water content in the membrane [29]

$$n_{drag} = n_{drag}^{SAT} \frac{\lambda}{22} \qquad \text{for } 0 \leq \lambda \leq 22 \tag{42}$$

where $n_{drag}^{SAT} \approx 2.5$. Consequently, the molar flux of water in the membrane due to the electro-osmotic drag will depend on the reaction rate

$$J_{H_2O}^{drag}(t) = 2n_{drag} \frac{j(t)}{2F} \tag{43}$$

where $J_{H_2O}^{drag}$ is the molar flux of water in the membrane (mol/s·m^2) and the quantity $2F$ converts from current density to proton flux [29]. The net water flux in the membrane is a combination of the electrosmotic drag and back diffusion

$$J_{H_2O}^{net} = J_{H_2O}^{drag} - \frac{\rho_{dry}}{M_m} D_\lambda(\lambda) \frac{d\lambda}{dx} \tag{44}$$

Equation (44) can be rewritten as

$$\frac{d\lambda}{dx} = \left(2n_{drag}^{SAT} \frac{\lambda(x)}{22} - \alpha \right) \frac{jM_m}{2F\rho_{dry}D_\lambda} \tag{45}$$

where x is the distance within the MEA (m) and α is an unknown parameter that denotes the ratio of water flux to hydrogen flux flowing through the membrane from anode to cathode. Solving equation (45) for λ in order to determine the water content as a function of the membrane's thickness yields

$$\lambda(x) = \frac{11\alpha}{n_{drag}^{SAT}} + C\exp\left(\frac{jM_m n_{drag}^{SAT}}{22F\rho_{dry}D_\lambda}x\right) \tag{46}$$

where C is a constant to be determined from the boundary conditions, i.e., the water content in the cathode and anode side.

2.4 Right Bipolar Plate. Similar to the heat balance for the left bipolar plate, the heat balance for the right bipolar plate is

$$\frac{dT_{BPP}^R(t)}{dt} = \frac{Q_{BPP,EP}^S(t) + Q_{air\_BPP}^R(t) - Q_{BPP,MEA}^R(t) + Q_{BPP}^{res}(j)}{\tau_{BPP}} \tag{47}$$

where T_{BPP}^R is the right bipolar plate temperature (K). The terms in equation (47) are

$$Q_{BPP,EP}^S(t) = \frac{A_{BPP}^S}{R_{EP,BPP}^"}\left(T_{EP}^R(t) - T_{BPP}^R(t)\right) \tag{48}$$

$$Q_{air\_BPP}^R(t) = h_{chan}A_{BPP}^V\left(T_{air}^R(t) - T_{BPP}^R(t)\right) \tag{49}$$

where T_{EP}^R is the right end plate temperature (K) and T_{air}^R is the air temperature in the channels of the right bipolar plate (K).

2.5 Right End Plate. Similar to the heat balance for the left end plate, the heat balance for the right bipolar plate is

$$\frac{dT_{EP}^R(t)}{dt} = \frac{Q_{surr}^R(t) + Q_{air\_EP}^V(t) - Q_{BPP,EP}^S(t)}{\tau_{EP}} \tag{50}$$

The terms in equation (53) are

$$Q_{surr}^R(t) = h_{surr}A_{EP}\left(T_0 - T_{EP}^R(t)\right) \tag{51}$$

$$Q_{air\_EP}^V(t) = h_{chan}A_{EP}^V\left(T_{air}^R(t) - T_{EP}^R(t)\right) \tag{52}$$

where $A_{EP}^V = a^V w_{BPP}$ is the total area of the end plate in contact with the air flowing through the channel (m^2).

2.6 Air Cooling. The energy balance for the air in the channels in the left bipolar plate is

$$\tau_{air} \frac{dT_{air}(t)}{dt} = \dot{m}_{air} c_{air} \left(T_{air,in} - T_{air,out}(t) \right) + h_{chan} A_{BPP}^V \left(T_{BPP}^L(t) - T_{air}^L(t) \right) \tag{53}$$
$$+ h_{chan} A_{MEA}^V \left(T_{MEA}(t) - T_{air}^L(t) \right)$$

where $\dot{m}_{air}$ is the air mass flow rate in the channels (g/s), c_{air} is the specific heat capacity of air (J/gK), $T_{air,in}$ is the air temperature at the channel inlet (298 K) and $T_{air,out}$ is the air temperature at the channel outlet (K). It is assumed that

$$T_{air}^L(t) \cong \frac{1}{2} \left(T_{air,in} + T_{air,out}(t) \right) \tag{54}$$

Since air has a considerably smaller thermal mass than any solid ($\sim 10^6$ times smaller), it is assumed that its thermal dynamics are significantly faster than those in the fuel cell layers and

$$\tau_{air} \frac{dT_{air}(t)}{dt} \simeq 0 \tag{55}$$

Therefore, the temperature of the air in the channels is assumed to change instantaneously and, hence, the air energy balance for the channels between the left bipolar plate and MEA is

$$0 = -2\dot{m}_{air} c_{air} T_{air}^L(t) + h_{chan} A_{BPP}^V \left(T_{BPP}^L(t) - T_{air}^L(t) \right) + h_{chan} A_{MEA}^V \left(T_{MEA}(t) - T_{air}^L(t) \right) \tag{56}$$

Similarly, the air energy balance for the channels between the right bipolar plate and the right end plate is

$$0 = -2\dot{m}_{air} c_{air} T_{air}^R(t) + h_{chan} A_{BPP}^V \left(T_{BPP}^R(t) - T_{air}^R(t) \right) + h_{chan} A_{EP}^V \left(T_{EP}^R(t) - T_{air}^R(t) \right) \tag{57}$$

Equations (56) and (57) allow for the mismatch of heat transfer to/from the solid surfaces forming the channels. Solving equations (56) and (57) for the air temperatures, respectively, and assuming that $T_{air,\,in} = T_0$ yields

$$T_{air}^L(t) = \frac{2\dot{m}_{air}c_{air}T_0 + h_{chan}A_{BPP}^V T_{BPP}^L(t) + h_{chan}A_{MEA}^V T_{MEA}(t)}{2\dot{m}_{air}c_{air} + h_{chan}\left(A_{BPP}^V + A_{MEA}^V\right)} \tag{58}$$

$$T_{air}^R(t) = \frac{2\dot{m}_{air}c_{air}T_0 + h_{chan}A_{BPP}^V T_{BPP}^R(t) + h_{chan}A_{EP}^V T_{EP}^R(t)}{2\dot{m}_{air}c_{air} + h_{chan}\left(A_{BPP}^V + A_{EP}^V\right)} \tag{59}$$

Rearranging equations (3), (10), (21), (47) and (50), and substituting T_{air}^L and T_{air}^R into equations (10), (21), (47) and (50) yields

$$\tau_{EP}\frac{dT_{EP}^L(t)}{dt} = a_{11}T_{EP}^L(t) + a_{21}T_{BPP}^L(t) + b_1 \tag{60}$$

$$\tau_{BPP}\frac{dT_{BPP}^L(t)}{dt} = a_{21}T_{EP}^L(t) + a_{22}T_{BPP}^L(t) + a_{23}T_{MEA}(t) + b_2 \tag{61}$$

$$\tau_{MEA}\frac{dT_{MEA}(t)}{dt} = a_{23}T_{BPP}^L(t) + a_{33}T_{MEA}(t) + a_{34}T_{BPP}^R(t) + b_3 \tag{62}$$

$$\tau_{BPP}\frac{dT_{BPP}^R(t)}{dt} = a_{43}T_{MEA}(t) + a_{44}T_{BPP}^R(t) + a_{45}T_{EP}^R(t) + b_4 \tag{63}$$

$$\tau_{EP}\frac{dT_{EP}^R(t)}{dt} = a_{54}T_{BPP}^R(t) + a_{55}T_{EP}^R(t) + b_5 \tag{64}$$

where

$$a_{11} = -h_{surr}A_{EP}^L - \frac{A_{BPP}^S}{R_{EP,BPP}^{"}} \tag{65}$$

$$a_{12} = \frac{A_{BPP}^S}{R_{EP,BPP}^{"}} \tag{66}$$

$$a_{21} = \frac{A_{BPP}^L}{R_{1,2}^{"}} \tag{67}$$

$$a_{22} = h_{chan}\left(\dot{m}_{air}\right) A_{BPP}^V \left(\frac{h_{chan}\left(\dot{m}_{air}\right) A_{BPP}^V}{2\dot{m}_{air} c_{air} + h_{chan}\left(\dot{m}_{air}\right) A_{BPP}^V + h_{chan}\left(\dot{m}_{air}\right) A_{MEA}^V} - 1 \right) - \frac{A_{BPP}^L}{R_{EP,BPP}^{"}} - \frac{A_{BPP}^S}{R_{EP,BPP}^{"}} \tag{68}$$

$$a_{23} = h_{chan}\left(\dot{m}_{air}\right) A_{BPP}^V \left(\frac{h_{chan}\left(\dot{m}_{air}\right) A_{MEA}^V}{2\dot{m}_{air} c_{air} + h_{chan}\left(\dot{m}_{air}\right) A_{BPP}^V + h_{chan}\left(\dot{m}_{air}\right) A_{MEA}^V} \right) + \frac{A_{BPP}^S}{R_{EP,BPP}^{"}} \tag{69}$$

$$a_{32} = \frac{A_{BPP}^S}{R_{BPP,MEA}^{"}} + h_{chan}\left(\dot{m}_{air}\right) A_{MEA}^V \left(\frac{h_{chan}\left(\dot{m}_{air}\right) A_{BPP}^V}{2\dot{m}_{air} c_{air} + h_{chan}\left(\dot{m}_{air}\right) A_{BPP}^V + h_{chan}\left(\dot{m}_{air}\right) A_{MEA}^V} \right)$$
$$- J_{H_2O}^{net} A_{MEA} MW_{H_2O} c_{H_2O} - \dot{m}_{O_2} c_{O_2} \tag{70}$$

$$a_{33} = h_{chan}\left(\dot{m}_{air}\right) A_{MEA}^V \left(\frac{h_{chan}\left(\dot{m}_{air}\right) A_{MEA}^V}{2\dot{m}_{air} c_{air} + h_{chan}\left(\dot{m}_{air}\right) A_{BPP}^V + h_{chan}\left(\dot{m}_{air}\right) A_{MEA}^V} - 1 \right)$$
$$- \frac{A_{BPP}^L}{R_{BPP,MEA}^{"}} - \frac{A_{BPP}^S}{R_{BPP,MEA}^{"}} + i\left[\frac{\Delta s}{n_e F} - \frac{R}{n_e F} \ln\left(\frac{\Pi a_P^{v_i}}{\Pi a_R^{v_i}} \right) \right] + \dot{m}_{O_2} c_{O_2} + \dot{m}_{H_2} c_{H_2} \tag{71}$$

$$a_{34} = \frac{A_{BPP}^L}{R_{BPP,MEA}^{"}} + \dot{m}_{H_2} c_{H_2} + J_{H_2O}^{net} A_{MEA} MW_{H_2O} c_{H_2O} \tag{72}$$

$$a_{43} = \frac{A_{BPP}^L}{R_{BPP,MEA}^{"}} \tag{73}$$

$$a_{44} = h_{chan}\left(\dot{m}_{air}\right) A_{BPP}^V \left(\frac{h_{chan}\left(\dot{m}_{air}\right) A_{BPP}^V}{2\dot{m}_{air} c_{air} - h_{chan}\left(\dot{m}_{air}\right)\left(A_{BPP}^V + A_{EP}^V\right)} - 1 \right) - \frac{A_{BPP}^L}{R_{BPP,MEA}^{"}} - \frac{A_{BPP}^S}{R_{BPP,EP}^{"}} \tag{74}$$

$$a_{45} = h_{chan}\left(\dot{m}_{air}\right) A_{BPP}^V \left(\frac{h_{chan}\left(\dot{m}_{air}\right) A_{EP}^V}{2\dot{m}_{air} c_{air} - h_{chan}\left(\dot{m}_{air}\right)\left(A_{BPP}^V + A_{EP}^V\right)} \right) + \frac{A_{BPP}^S}{R_{BPP,EP}^{"}} \tag{75}$$

$$a_{54} = \frac{A_{BPP}^S}{R_{EP,BPP}^{"}} + h_{chan}\left(\dot{m}_{air}\right) A_{EP}^V \left(\frac{h_{chan}\left(\dot{m}_{air}\right) A_{BPP}^V}{2\dot{m}_{air} c_{air} - h_{chan}\left(\dot{m}_{air}\right)\left(A_{BPP}^V + A_{EP}^V\right)} \right) \tag{76}$$

$$a_{55} = h_{chan}\left(\dot{m}_{air}\right)A_{EP}^{V}\left(\frac{h_{chan}\left(\dot{m}_{air}\right)A_{EP}^{V}}{2\dot{m}_{air}c_{air} - h_{chan}\left(\dot{m}_{air}\right)\left(A_{BPP}^{V} + A_{EP}^{V}\right)} - 1\right) - h_{surr}A_{EP} - \frac{A_{BPP}^{S}}{R_{EP,BPP}^{"}} \quad (77)$$

$$b_{1} = h_{surr}A_{EP}^{L}T_{0} \quad (78)$$

$$b_{2} = h_{chan}\left(\dot{m}_{air}\right)A_{BPP}^{V}\left(\frac{2\dot{m}_{air}c_{air}}{2\dot{m}_{air}c_{air} + h_{chan}\left(\dot{m}_{air}\right)\left(A_{BPP}^{V} + A_{MEA}^{V}\right)}\right)T_{0} + i^{2}\frac{\rho_{BPP}^{res}l_{BPP}}{A_{BPP}^{L}} \quad (79)$$

$$b_{3} = h_{chan}\left(\dot{m}_{air}\right)A_{MEA}^{V}\left(\frac{2\dot{m}_{air}c_{air}}{2\dot{m}_{air}c_{air} + h_{chan}\left(\dot{m}_{air}\right)A_{BPP}^{V} + h_{chan}\left(\dot{m}_{air}\right)A_{MEA}^{V}}\right)T_{0}$$
$$+ i^{2}\frac{\rho_{MEA}^{res}\left(\lambda\right)l_{MEA}}{A_{MEA}} - jA_{MEA}\left(\eta\left(j\right)\right) \quad (80)$$

$$b_{4} = h_{chan}\left(\dot{m}_{air}\right)A_{BPP}^{V}\left(\frac{2\dot{m}_{air}c_{air}}{2\dot{m}_{air}c_{air} - h_{chan}\left(\dot{m}_{air}\right)\left(A_{BPP}^{V} + A_{EP}^{V}\right)}\right)T_{0} + i^{2}\frac{\rho_{BPP}^{res}l_{BPP}}{A_{BPP}^{L}} \quad (81)$$

$$b_{5} = \left[h_{surr}A_{EP} + h_{chan}\left(\dot{m}_{air}\right)A_{EP}^{V}\left(\frac{2\dot{m}_{air}c_{air}}{2\dot{m}_{air}c_{air} - h_{c}\left(\dot{m}_{air}\right)\left(A_{BPP}^{V} + A_{EP}^{V}\right)}\right)\right]T_{0} \quad (82)$$

The thermal model can now be expressed in matrix form as

$$\dot{\mathbf{T}}(t) = \mathbf{A}\mathbf{T}(t) + \mathbf{B} \quad (83)$$

where

$$\mathbf{A} = \begin{bmatrix} \dfrac{a_{11}}{\tau_{1}} & \dfrac{a_{12}}{\tau_{1}} & 0 & 0 & 0 \\[2ex] \dfrac{a_{21}}{\tau_{2}} & \dfrac{a_{22}}{\tau_{2}} & \dfrac{a_{23}}{\tau_{2}} & 0 & 0 \\[2ex] 0 & \dfrac{a_{32}}{\tau_{3}} & \dfrac{a_{33}}{\tau_{3}} & \dfrac{a_{34}}{\tau_{3}} & 0 \\[2ex] 0 & 0 & \dfrac{a_{43}}{\tau_{4}} & \dfrac{a_{44}}{\tau_{4}} & \dfrac{a_{45}}{\tau_{4}} \\[2ex] 0 & 0 & & \dfrac{a_{54}}{\tau_{5}} & \dfrac{a_{55}}{\tau_{5}} \end{bmatrix} \quad (84)$$

$$\mathbf{B} = \begin{bmatrix} \dfrac{b_1}{\tau_1} & \dfrac{b_2}{\tau_2} & \dfrac{b_3}{\tau_3} & \dfrac{b_4}{\tau_4} & \dfrac{b_5}{\tau_5} \end{bmatrix}^T \qquad (85)$$

$$\mathbf{T} = \begin{bmatrix} T_1 & T_2 & T_3 & T_4 & T_5 \end{bmatrix}^T \qquad (86)$$

2.7 N-cell Stack Model. By modifying the same structure that was followed for the single cell model, the thermal model for an n-cell stack can be determined. Figure 5 illustrates the configuration of an n-cell stack.
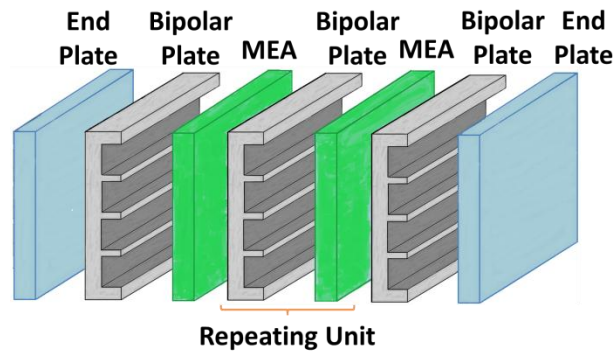
Fig. 5. N-cell stack configuration.

The number of layers (n_{layers}) in the thermal model is related to the number of cells (n_{cells}) in the stack by

$$n_{layers} = 2n_{cells} + 3 \qquad (87)$$

Since the layers forming the stack are the same as the ones forming the unit cell, the equations used to form the model are the same. This yields a system of n_{layers} equations with n_{layers} states, each of which describes the temperature of a specific component in the fuel cell stack.

3 Physical System

      The hydrogen fuel cell model parameters for the simulation studies conducted in this paper are from a commercially available fuel cell, the Horizon H-200, shown in Figure 6. The fuel cell maximum power is 200 W with a maximum amperage of 8 A. The stack consists of 48 cells. The bipolar plates are constructed from graphite and the end plates from aluminum. Also, as described previously, the polymer electrolyte membrane is Nafion®. The configuration of this fuel cell is typical of an air breathing fuel cell, having an open cathode that feeds off of the air provided by the channels in the bipolar plates. Each bipolar plate consists of 56 air channels. These air streams also serve as a cooling system for this fuel cell system. Due to the limitations in the fans speed, the maximum air flow rate that can be moved through an individual cell is 1.1×10^{-3} g/s. The maximum hydrogen flow rate that can be fed into the fuel cell is 1.5×10^{-2} g/s. This study, however, will only consider the amount of hydrogen that the fuel cell requires to operate at each current demand ($0\text{-}4 \times 10^{-3}$ g/s). Another important characteristic of these fuel cells is that due to their open-cathode assembly, the cathode pressure will remain fixed at 1 atm. In order to keep the membrane from deforming, the anode pressure will also be kept at atmospheric pressure. The densities and specific heat capacities of the fuel cell materials are shown in Table 1.

Fig. 6. Horizon H-200 fuel cell stack.

Table 1 Specific heat capacities and densities of H-200 fuel cell materials.

	Density (kg/m^3)	Specific heat capacity (J/kg·K)
End Plate (Al)	2705	900
Bipolar Plate (Graphite)	1625	770
MEA	1800	872

Note the MEA consists of two catalyst layers each (one for the anode and one for the cathode), two gas diffusion layers (GDL), one for the anode and cathode sides, and one Nafion® membrane. In order to obtain the MEA density and specific heat capacity, the effective properties for the MEA are calculated with the values for each of these layers, as shown in Table 2. The measured areas for the fuel cell used for the simulation studies in this paper are shown in Table 3.

Table 2 Densities, specific heat capacities and layer volume of materials forming the MEA layer [18].

	Density (kg/m^3)	Specific heat capacity (J/kg·K)	Layer Volume (m^3)
Anode/Cathode GDL	2000	840	5.90×10^{-6}
Anode/Cathode catalyst layer	387	770	9.59×10^{-7}
Membrane (Nafion®)	1970	1100	1.87×10^{-6}

Table 3 Fuel cell areas of each heat transfer interface in the different layers.

Layer	Wet Area (m^2)	Solid Channel Area (m^2)	Solid Surface Area (m^2)
Left End Plate	1.447×10^{-3}	1.596×10^{-3}	6.522×10^{-3}
Left Bipolar Plate	7.599×10^{-3}	1.596×10^{-3}	3.044×10^{-3}
MEA	3.044×10^{-3}	1.596×10^{-3}	3.044×10^{-3}
Right Bipolar Plate	7.599×10^{-3}	1.596×10^{-3}	3.044×10^{-3}
Right End Plate	1.447×10^{-3}	1.596×10^{-3}	6.522×10^{-3}

The thermal contact resistances between the materials that form the MEA are between 2.0×10^{-4} and 6.7×10^{-4} m$^2 \cdot$K/W [32], and the thermal contact resistance between the bipolar plates and the MEA is 2.0×10^{-4} m$^2 \cdot$K/W [32]. Thermal contact resistances depend on surface finish and the pressure under which the fuel cell layers are clamped together. It is then approximated that the thermal contact resistances are the same for all layer interfaces throughout the stack. For the simulation studies conducted in this paper, all thermal contact resistances are assumed to be 2.0×10^{-4} m$^2 \cdot$K/W.

In order to determine the heat generated in the MEA, the individual cell polarization curve is constructed (Figure 7). The experimental data is obtained by measuring the fuel cell voltage as different currents are drawn from the fuel cell by means of a programmable load (BK Precission 8502 300W Programmable DC Electronic load). The total voltage is then divided by the number of cells in order to determine an approximate nominal polarization curve for each cell.
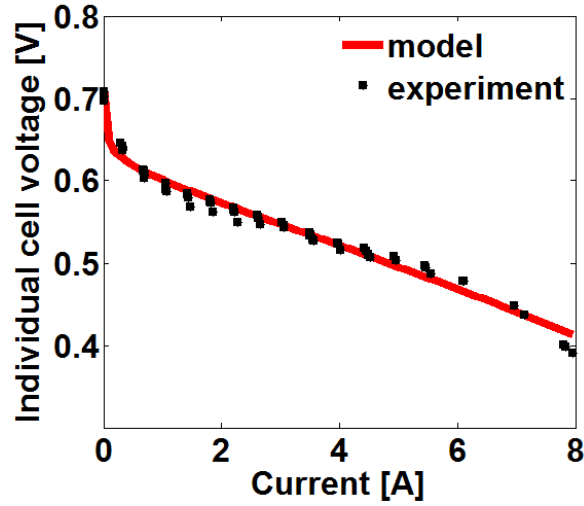
Fig. 7. Horizon H-200 single cell experimental polarization curve.

An optimization method known as Particle Swarm Optimization (PSO) [33] is used to create a model of the single cell polarization curve. Given the experimental data shown in Figure 8, the model parameters in equation (37) are optimized such that the difference between the model outputs and corresponding experimental data is minimized. The PSO method yields

$$
\begin{aligned}
E_{total}(t) &= E_{thermo}(t) - A\ln\left(\frac{i(t)}{A_{active}}\right) - R\frac{i(t)}{A_{active}} - m\,e^{n\frac{i(t)}{A_{active}}} \\
&= 1.202 - 1.261\times10^{-3}\ln\left(\frac{i(t)}{14.22}\right) - 0.6817\frac{i(t)}{14.22} - 0.6162\exp\left(-0.7099\frac{i(t)}{14.22}\right)
\end{aligned}
\tag{88}
$$

where A_{active} is the fuel cell active area (cm^2). From the results obtained from the polarization curve, it can be determined that $A_{active} = 14.22$ cm^2. This value can be validated from the fuel cell stack sizing graph in the literature [26] where it is inferred that for fuel cell stacks with less than 1 kW power and 50 cells, the active area is ≤ 25 cm^2. Also, the fuel cell area normalized fuel cell resistance is 0.6817 Ω·cm^2. This parameter is comparable to the ranges given in the literature (0.1155 Ω·cm$^2 \leq R \leq 0.6195$ Ω·cm^2) [1].

Since the ideal thermodynamic voltage is temperature dependent, this term was expanded as defined previously in equation (30). Note there are two electrons involved in the reaction ($n^e = 2$), $T_0 = 298$ K , $R = 8.314$ J/mol·K, $F = 96485.34$ C/mol and $\Delta s =$ 0.104 and -323.36 J/mol·K for the anode and cathode reactions, respectively [31]. Since the cathode reaction energy is three orders of magnitude greater than that of the anode, only the entropy of the cathode is taken into consideration [31]. Also note that in order to compute E_{thermo}, since the anode and cathode pressures are 1 atm and oxygen represents 21% or the air entering the fuel cell, equation (31) becomes

$$E_{thermo}(t) = 1.23 + \frac{-326.36}{2(96485.34)}\left(T_{MEA}(t) - 298\right) - \frac{8.314 T_{MEA}(t)}{2(96485.34)} \ln\left(\frac{1}{\sqrt{0.21}}\right) \qquad (89)$$

From the terms obtained in equations (88), (89) and (35), the individual heat source terms for the membrane can be found and compared. The different heat generation terms are plotted as a function of current in Figure 8 and compared to the total heat generation in the MEA.
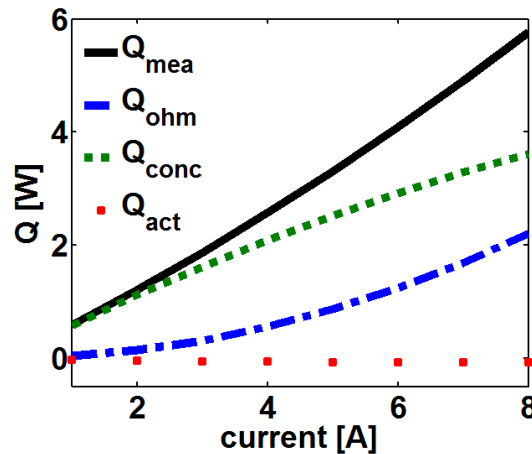

Fig. 8. Heat generation from different sources and total MEA internal heat generation versus current.

Often in the literature the concentration and activation losses are lumped together as one "activation" term. In this paper, however, these two terms have been considered separately in order to study their effects independently. As seen in Figure 8, from the parameters obtained through the polarization curve, the activation process is an endothermic event where the electrochemical reaction is absorbing heat energy in order to occur. This is why operating the fuel cell at higher temperatures will favor the reaction and produce higher power, assuming optimum membrane hydration. Also, comparing this term to the other heat generation terms, it is determined that the activation energy term can be ignored. Lastly, the electrical resistivity of graphite is 1.75×10^{-5} Ω·m and the bipolar plate thickness is 2.7 mm. Referring to equation (14), the heat generated in the bipolar plates is

$$Q_{BPP}^{res}(t) = \frac{\rho_{res}l_{BPP}}{A_{BPP}}i(t)^2 = 1.552\times10^{-5}i(t)^2 \tag{90}$$

4 Steady State Analysis

4.1 One-cell Steady State Model.
In the steady state, equation (87) is

$$\mathbf{A}_{ss}\mathbf{T}+\mathbf{B}_{ss} = \mathbf{0} \tag{91}$$

where

$$\mathbf{A}_{ss} = \begin{bmatrix} a_{11} & a_{12} & 0 & 0 & 0 \\ a_{21} & a_{22} & a_{23} & 0 & 0 \\ 0 & a_{32} & a_{33} & a_{34} & 0 \\ 0 & 0 & a_{43} & a_{44} & a_{45} \\ 0 & 0 & 0 & a_{54} & a_{55} \end{bmatrix} \tag{92}$$

$$\mathbf{B}_{ss} = \begin{bmatrix} b_1 & b_2 & b_3 & b_4 & b_5 \end{bmatrix}^T \tag{93}$$

From the fuel cell-fan operation, the maximum flow rate that can be provided to the fuel cell is 1.39 L/min. The Reynolds number obtained for the flow in each channel is smaller

than 650 for the entire range of fan operation. Therefore, the flow in the channels will remain laminar for the entire range of fan speeds and $h_c = 69.24 \text{W/m}^2 \cdot \text{K}$.

As previously mentioned, the membrane is considered to be fully hydrated; thus, it can be assumed that the membrane is fully saturated, i.e., $\dfrac{d\lambda(x)}{dx} = 0$. In this case

$$J_{H_2O}^{net} = J_{H_2O}^{drag} = 1.822 \times 10^{-6} i(t) \tag{94}$$

Substituting this result into equation (25), the water enthalpy is

$$\Delta H_{H_2O}(t) = 1.822 \times 10^{-6} i(t) \left(T_{BPP}^{R}(t) - T_{BPP}^{L}(t) \right) \tag{95}$$

The enthalpies of hydrogen and oxygen, respectively, are

$$\Delta H_{H_2}(t) = 1.492 \times 10^{-4} j(t) \left(T_{MEA}(t) - T_{BPP}^{R}(t) \right) \tag{96}$$

$$\Delta H_{O_2}(t) = 7.711 \times 10^{-5} j(t) \left(T_{MEA}(t) - T_{BPP}^{L}(t) \right) \tag{97}$$

Moreover, with the specific material and geometric values previously given, it can be determined that the heat transferred by conduction from the left bipolar plate to the MEA is the same as the heat transferred by conduction from the right bipolar plate to the right end plate (3.669 W/K). Similarly, the heat transferred by conduction between the left end plate and the left bipolar plate is the same as the heat transferred between the MEA and the right bipolar plate (6.9977 W/K). The heat transfer convection coefficient with the surrounding air is 20 W/m²·K, yielding a heat transfer by convection from the environment to the right and left end plates of 0.1304 W/K. Also, due to geometric similarities, the denominators of all the convection terms are the same (i.e., $2.4\dot{m}_{air} + 0.6265$). In order to maximize the terms that appear in the $\mathbf{A_{ss}}$ matrix as a function of inputs, i.e., current and mass flow rate, the maximum available current in the fuel cell and the minimum air mass flow rate are substituted into the terms of the $\mathbf{A_{ss}}$ matrix. When all of the terms in the $\mathbf{A_{ss}}$ matrix are compared, it is found that the enthalpy terms, the convection terms and the MEA heat generation terms are at least one order of magnitude smaller than the conduction terms. Neglecting these terms

$$
\mathbf{A}_{ss} = \begin{bmatrix}
-6.9977 & 6.9977 & 0 & 0 & 0 \\
6.9977 & -6.9977-3.669 & 3.669 & 0 & 0 \\
0 & 3.669 & -6.9977-3.669 & 6.9977 & 0 \\
0 & 0 & 6.9977 & -6.9977-3.669 & 3.669 \\
0 & 0 & 0 & 3.669 & -3.669
\end{bmatrix} \quad (98)
$$

The matrix $\mathbf{A}_{ss}$ is singular when the mentioned terms are neglected and hence, the steady state temperatures cannot be computed. Therefore, the errors in the steady state solution will be analyzed for different simplifications where these terms will be neglected in different combinations.

In order to perform the steady state analysis, the terms forming matrix $\mathbf{B}_{ss}$ will also be studied. Examining the terms in the $\mathbf{B}_{ss}$ matrix two terms can be distinguished in the rows corresponding to the bipolar plates' energy balances, i.e., 2nd and 4th rows: a convection term and a heat generation term. The first term depends on the mass flow rate of air going through the channels, while the second term depends on the current going through the bipolar plate. Hence, the first term results in a minimum and maximum value of 3.4×10^{-2} and 0.340 W, respectively. On the other hand, the heat generated by the bipolar plate is between 0 and 1.552×10^{-4} W. Comparing these results it is determined that the heat generated by the bipolar plates is insignificant compared to the energy dissipated by convection by the air flowing through the bipolar plate channels and, hence, the heat generation term can be neglected.

To ensure the simplifications previously mentioned are valid, the steady state temperatures are computed for multiple operating currents (1-8 A) and air mass flow rates (5.66×10^{-5}-5.66×10^{-4} g/s). These ranges were determined by the physical limitations of the Horizon fuel cell. The steady state analysis is performed for different scenarios were each term indicated in Table 4 was included or not in the analyses. Comparing each case described in Table 4 to the analysis where all the terms are included, the errors in the steady state solutions obtained from neglecting the different terms in the system are obtained and shown in Table 4.

Table 4 Percent error in steady state temperatures for 1 cell neglecting enthalpies, air mass flow rates and/or heat generation in the bipolar plates.

Case #	Maximum % (ΔT_{ss})	Negligible Terms		
		ΔH	Convection terms in A_{ss}	Q_{BPP}^{res}
Case 1	0	Included	Included	Included
Case 2	1.06	Included	Not Included	Not Included
Case 3	1.06	Included	Not Included	Included
Case 4	3.81×10^{-4}	Included	Include	Not Included
Case 5	0.912	Not Included	Included	Included
Case 6	Cannot compute	Not Included	Not Included	Not Included
Case 7	Cannot compute	Not Included	Not Included	Included
Case 8	0.913	Not Included	Included	Not Included

As previously mentioned, the denominator in all of the convection terms is $2.4\dot{m}_{air}+0.6265$. The first term in this denominator is at least two orders of magnitude smaller than the second one. Since cases 6 and 7 in Table 4 cannot be computed due to A_{ss} being singular, the analysis was repeated ignoring only the air mass flow rate-dependent term in the denominator in matrices A_{ss} and B_{ss} instead of the entire convection terms in A_{ss}. Comparing the results obtained proceeding with this analysis to the results shown in Table 4, the error in all the cases can be computed, i.e., A_{ss} will not be singular in any case. The errors in cases 1-5 and case 8 do not change from the values calculated in Table 4. However, cases 6 and 7 now yield 0.95% error compared to the steady state solution obtained without neglecting any term.

The analysis illustrates that due to the small heat storage capability of gases, the changes in enthalpy of the reactant and product species do not contribute considerably to the heat transfer problem and can be ignored. Further, it is observed that the heat generated by the bipolar plate is negligible compared to the other terms in the energy

balance and can be neglected. Studying the percent error obtained in the steady state solution, it could also be concluded that neglecting the air mass flow rate in the denominators of all the convection terms in the analysis would not affect the results noticeably since the error introduced ignoring this term is ~1%. However, neglecting this denominator term yields an increase in the steady state temperatures as the air mass flow rate is increased. Since this result does not make physical sense, the air mass flow rate will not be neglected in any term of the model.

4.2 Heat Exchanger Analogy. In order to validate the steady state analysis, an analogy between the fuel cell and a heat exchanger is made. Assuming a parallel-flow heat exchanger (illustrated in Figure 9) with a heat source equal to the heat generated by the MEA and at a constant temperature T_s, the temperature of the air in the channels will exponentially tend to the temperature of the heat exchanger (i.e., the fuel cell temperature) as shown in Figure 10.
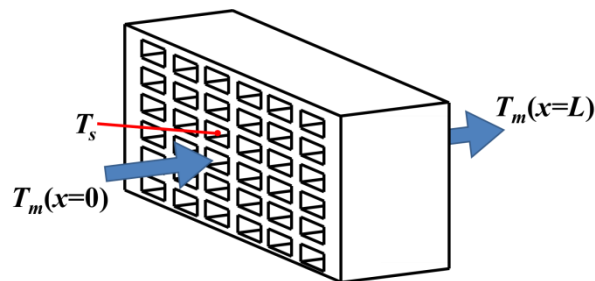

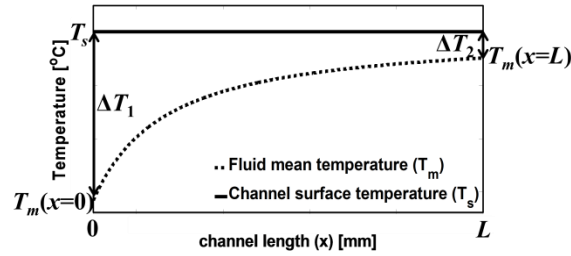Fig. 9. Heat exchanger schematic. The solid block is at a constant temperature (T_s).

Fig. 10. Temperature distribution forheat exchanger with constant wall temperature.

In Figure 10, $T_m(x)$ is the mean fluid temperature at different locations along the channel. As observed in Figures 13 and 14, the fluid enters the heat exchanger at a mean temperature $T_m(x = 0) = 298$ K and exits at a temperature $T_m(x = L)$. The temperature difference between the channel wall, which is the same as the fuel cell's bipolar plate temperature, and the air at the channel entrance is ΔT_1, and the temperature difference between the channel wall and the air at the channel outlet is ΔT_2. The air energy balance in the channel is

$$q = \dot{m}_{air} c_{p_{air}} \left(T_m(L) - T_m(0) \right) \tag{99}$$

where q is the heat dissipated by the fluid flow (W). Note that $T_m(L) - T_m(0) = \Delta T_2 - \Delta T_1$. For a parallel-flow heat exchanger [24]

$$q = Ah_c \frac{\Delta T_2 - \Delta T_1}{\ln(\Delta T_1 / \Delta T_2)} \tag{100}$$

where q is the heat generated by the heat exchanger (W) and A is the channel wet area (i.e., the channel perimeter times the channel length) (m^2). Equating equations (99) and (100) and rearranging

$$\frac{\Delta T_1}{\Delta T_2} = \exp\left(-\frac{Ah_c}{\dot{m}_{air} c_{p_{air}}} \right) \tag{101}$$

Note that since the fuel cell is being approximated as a heat exchanger, the heat generated by the MEA will be equal to the heat generated by the heat exchanger (q) and will also be the same as the heat dissipated by the air flowing across the channels. In order to analyze the temperature of the flow in each channel, the following assumption is made: the heat generated by the MEA will be evenly distributed in each channel. Therefore, assuming there are 56 channels in each bipolar plate and there is one bipolar plate at each side of the MEA, equation (99) becomes

$$q = \frac{Q_{MEA}^{int} / 2}{56} \tag{102}$$

This heat generation is divided into two terms: $Q_t = k_t T_{MEA}$ being the heat generation portion dependent on the temperature ($T_{MEA} = T_s$) and Q_l being the heat generation portion dependent on the ohmic, concentration and activation losses. Equating the heat transfer rate in equation (99) to the heat generated in the fuel cell and solving for $T_m(L)$ yields

$$T_m(L) = \frac{k_t T_s + Q_l}{\dot{m}_{air} c_{p_{air}}} + T_m(0) \tag{103}$$

Substituting equation (103) into equation (101) and solving for the fuel cell temperature yields

$$T_s = \frac{\dfrac{Q_l}{\dot{m}_{air} c_{p_{air}}} + (1 - E) T_m(0)}{1 - E - \dfrac{Q_t}{\dot{m}_{air} c_{p_{air}}}} \tag{104}$$

where

$$E = \exp\left(-\frac{A h_c}{\dot{m}_{air} c_{p_{air}}}\right) \tag{105}$$

Figure 11 compares the fuel cell temperatures obtained through the heat exchanger analysis to the steady state temperatures obtained from the model exchanging the end plates for adiabatic boundary conditions.
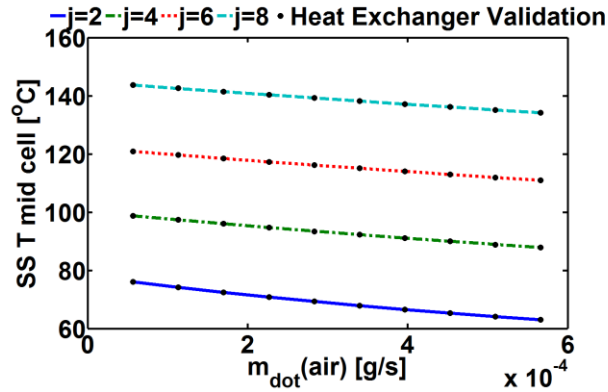
Fig. 11. Model fuel cell temperatures with no end plates and adiabatic boundary
conditions (lines) and heat exchanger temperatures (markers).

As seen in Figure 11, the parallel-flow heat exchanger temperature results
accurately match the steady state fuel cell model (0% for all data). The heat exchanger
analysis brings new insight to the study of fuel cells as a first-approach steady state
thermal model. A new reverse engineering perspective is now given to the design of fuel
cells: the heat generated in the fuel cell can be determined first given a desired operating
temperature. Knowing the heat generation in the fuel cell, the voltage losses can be
calculated, which will determine the specific characteristics of the desired fuel cell.

4.3 N-cell Stack Steady State Model. The single cell model can be extended to
form a fuel cell stack with higher wattage capabilities. The effects of neglecting the
enthalpy, heat generation in the bipolar plates or the mass flow rate of air terms in a 48-
cell stack is shown in Table 5.

Table 5 Percent error in steady state temperatures for 48-cell stacks neglecting enthalpies, air mass flow rates and/or heat generation in the bipolar plates.

Case #	Maximum % (ΔT_{ss})	Negligible Terms		
		ΔH	$\dot{m}_{air}$	Q_{BPP}^{res}
Case 1	0	Included	Included	Included
Case 2	28.5	Included	Not Included	Not Included
Case 3	28.5	Included	Not Included	Included
Case 4	2.44×10^{-3}	Included	Include	Not Included
Case 5	0.754	Not Included	Included	Included
Case 6	Cannot compute	Not Included	Not Included	Not Included
Case 7	Cannot compute	Not Included	Not Included	Included
Case 8	0.756	Not Included	Included	Not Included

Comparing Tables 4 and 5, it can be observed that most errors are amplified as the number of cells in the stack is increased. Also, similar to the single cell analysis, the air mass flow rate will be neglected in the denominator of the convection terms as a separate case study. It is observed that the error introduced by ignoring the air mass flow rate in the denominators increases by almost 27 times in the 48-cell stack versus the single cell stack (29% error in computation of the steady state temperatures). On the other hand, the error in the computation of the steady state temperatures introduced by neglecting the enthalpies and the heat generated by the bipolar plates remains under 1%, thus, these terms can be neglected.

In order to investigate the effects of different mass flow rates and operating currents on different size fuel cells, the steady state temperatures were computed for each fuel cell layer at different operating conditions. Figures 12 and13 show steady state fuel cell temperatures for 16 and 48-cell fuel cell stacks, respectively.
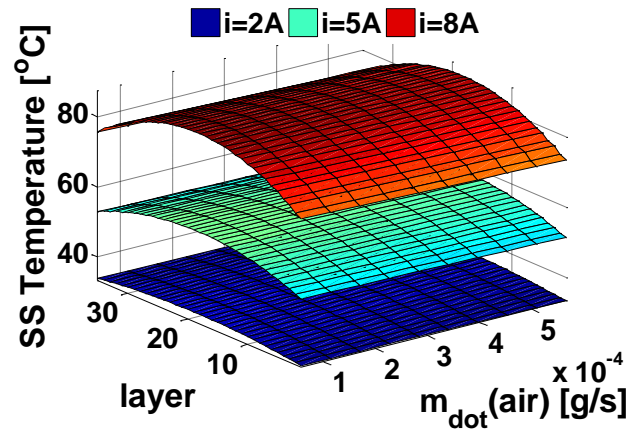
Fig. 12. Steady state temperature distribution as a function of mass flow rate and layer of a 16 cell-stack fuel cell operating at 2A, 5A and 8A.
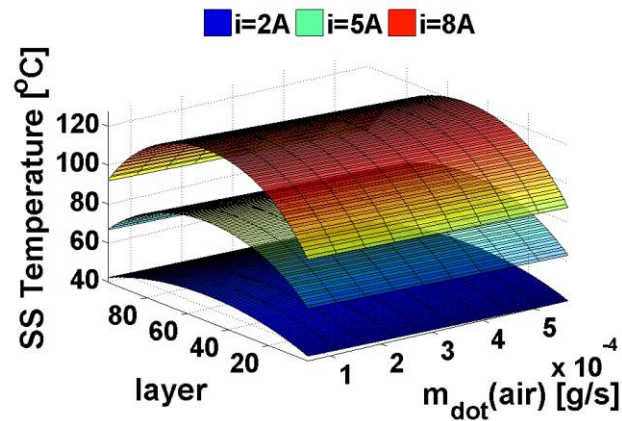

Fig. 13. Steady state temperature distribution as a function of air mass flow rate of a 48 cell-stack fuel cell operating at currents of 2, 5 and 8 A.

As Figures 12 and 13 illustrate, the temperature distribution of each stack has a parabolic shape in the steady state. These profiles show that the middle layer reaches the highest temperature and the end plates are the coldest areas. Due to the larger dimensions and material properties of the end plates, the thermal mass of these layers is two orders of

magnitude larger than those of the other layers. Greater thermal masses imply higher heat storage capacity. In addition, the heat from these layers is dissipated by convection to the environment. Thus, these two layers have the lowest temperatures. Since the middle layers are more insulated from the environment, the shape of the heat distribution is expected. Comparing the different sizes of fuel cells, it can be seen that the temperature distribution for the 48-cell stack encompasses a much wider range of values than the single cell fuel cell. As the number of layers increase, the temperature difference between the middle layer and the exterior of the stack also increases. Similarly, note that the maximum temperatures for one cell are lower than the maximum temperatures for a the 48-cell stack. This is due to the fact that, for the same current, larger fuel cells produce more energy (and therefore, more waste heat) as the power is approximately linearly scaled with the number of cells that form the stack. Again, comparing both fuel cells, it is observed that the 48-cell fuel cell is more affected by the air mass flow rate than the single-cell fuel cell.

Figures 12 and 13 also show that for a constant current, the maximum steady state temperatures linearly decrease with increasing mass flow rates. This observation is clearly illustrated in Figure 14.
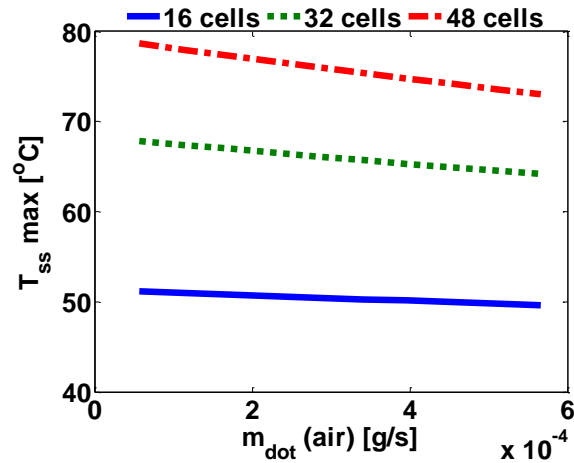
Fig. 14. Maximum steady state temperatures for different size fuel cell stacks operating at 4 A versus air mass flow rate per cell.

As Figure 14 shows, the maximum steady state temperature increases for increasing number of cells and is more sensitive for larger fuel cell stacks. Analysis shows the slopes of the curves in Figure 16 decrease linearly with increasing number of cells. The rate at which heat is dissipated by the increasing air mass flow rate increases approximately linearly with increasing number of cells.

Moreover, as Figures 12 and 13 illustrate, quadrupling the number of cells in the stack will significantly increase the overall stack temperatures, ~34% and ~42% for currents of 2 and 8 A operating conditions, respectively. These results can be more easily visualized in Figure 15.
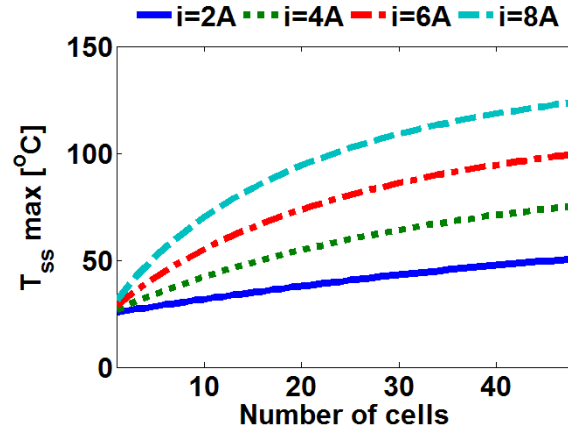
Fig. 15. Maximum steady state temperatures versus number of cells for 5.668×10^{-4} g/s per cell.

5 Dynamic Analysis

The fuel cell operation is simulated for different scenarios. In the first simulation, the air mass flow rate is kept constant at 2.86×10^{-5} g/s per cell. The fuel cell temperature is analyzed by varying its operating current as illustrated by Figure 16.

Each current step lasted long enough such that all of the layers reached their steady state temperatures. One-cell and 48-cell stack fuel cell responses were simulated for the same current input. Their dynamic temperature responses are illustrated in Figures 17 and 18, respectively.
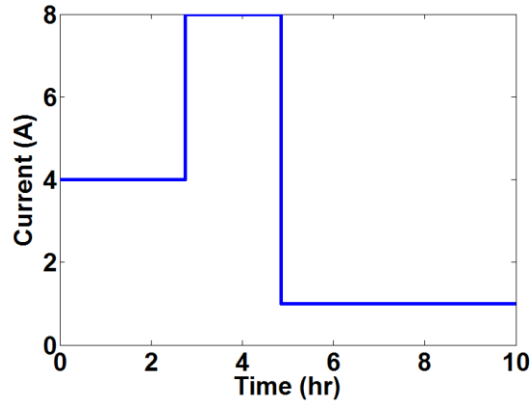
Fig. 16. Varying current input with time i = 4, 8 and 1 A.

Fig. 17.   Left end plate and middle MEA temperatures versus time. One-cell fuel cell temperature response to current input described by current profile in Figure 16 and $\dot{m}_{air} =$ 2.86×10^{-5} g/s per cell.

Comparing the middle MEA layer to the end plate one-cell stack temperature profiles, it can be observed that the end plate temperature settles down slightly after the middle MEA for the first two input steps and at the same time for the last step.
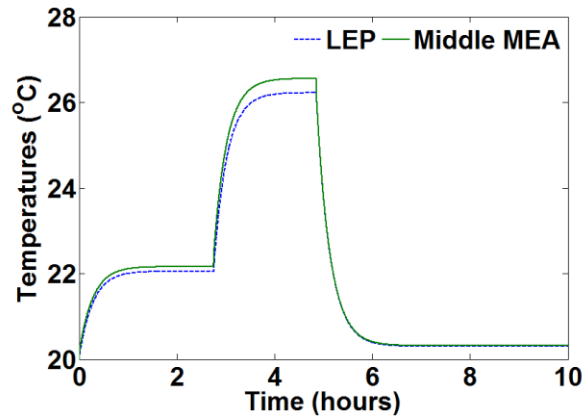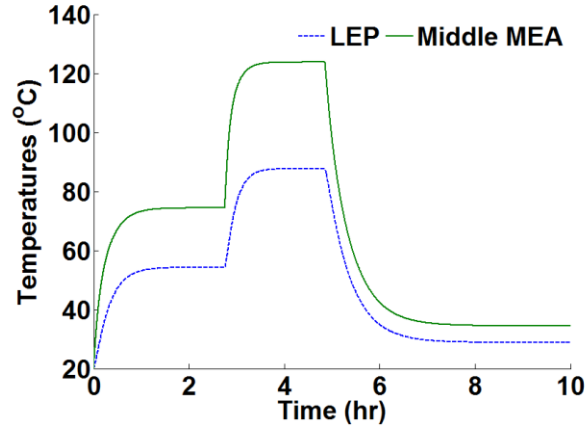
Fig. 18. Left end plate and middle MEA temperatures versus time. 48-cell fuel cell temperature response to current input described by current profile in Figure 16 and $\dot{m}_{air} =$ 2.86×10^{-5} g/s per cell.

Comparing the middle MEA layer to the end plate in the 48-cell stack temperature profiles, it can be observed that the settling time is, ~20% faster in the middle MEA than it is in the end plate when the system experiences a current input change. As seen in Figures 17 and 18, it takes about one hour for the fuel cell temperatures to reach their maximum values at the commanded current input. Comparing the dynamics of both simulations, it can be observed that for the first two steps of the simulation, the dynamics of the 48-cell stack are slower than those in the one-cell stack. However, the on the last step of the simulation, the one-cell stack settles down at a constant temperature in less time than the 48-cell stack. In order to quantify how these systems responded to the current change, the settling time for each temperature variation is given in Table 6 for both systems.

Table 6   Settling times (hours) for each temperature variation described in Figures 19 and 20.

Location	1 cell			48 cells		
	1 A	4 A	8 A	1 A	4 A	8 A
EP	1.10	1.09	1.06	1.75	1.32	0.94
Middle MEA	1.04	1.03	1.00	1.30	0.87	0.52

In the second simulation, the current is 4 A. The fuel cell temperature was analyzed by varying the air mass flow rate as shown in Figure 19.
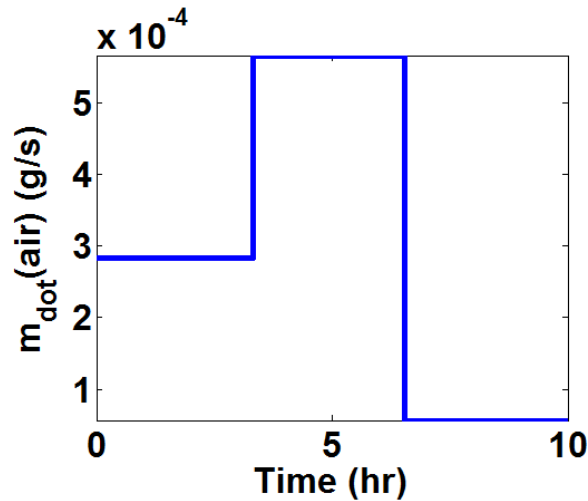

Fig. 19. Varying mass flow rate input with time $\dot{m}_{air} = 2.86\times10^{-5}$, 5.72×10^{-5} and 1.43×10^{-5} g/s per cell.

One-cell and 48-cell stack fuel cell responses were simulated for the mass flow rate input in Figure 19. Their dynamic temperature responses are given in Figures 20 and 21, respectively.

Fig. 20. Left end plate and middle MEA temperatures versus time.
One-cell fuel cell temperature response to the air mass rate input described by the profile
in Figure 21 with i = 4 A.

It is observed that the speed of response of the system temperature for the one-cell stack gets faster as the mass flow rate is increased. Also, is observed that, the end plate responds ~5% slower than the MEA to every change in mass flow rate.
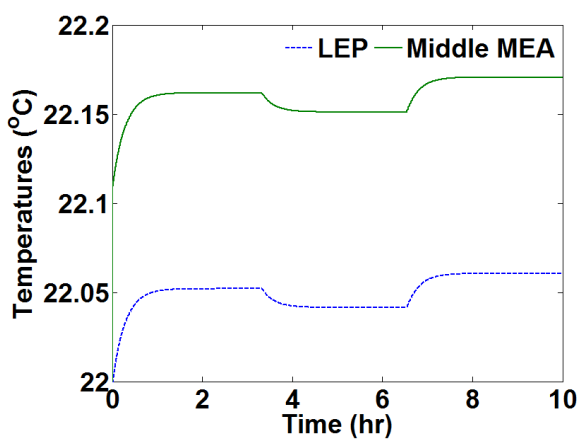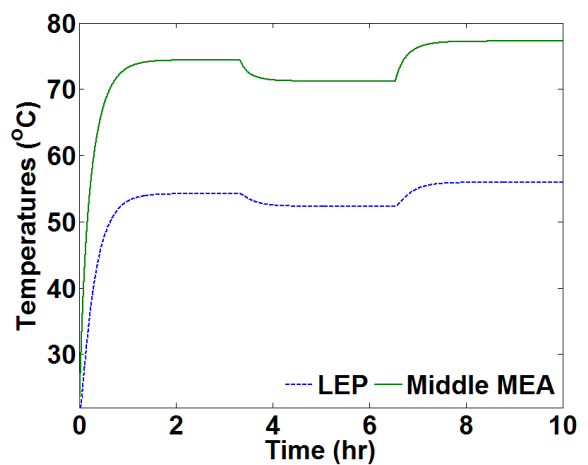

Fig. 21.   Left end plate and middle MEA temperatures versus time.
48-cell fuel cell temperature response to air mass flow rate input described by the profile
in Figure 21 and i = 4 A.

In the 48-cell stack, the difference between the speeds of response of the different layers is more noticeable. The end plate is ~70% slower than the middle MEA. Also, similar to the one-cell fuel cell, as the mass flow rate increases, the system settling time decreases (with a ~5% difference between the settling times for the smallest and the largest mass flow rates). The maximum temperature change experienced by the change in the air mass flow rate observed in Figure 20 is ~0.14°C, while the 48-cell fuel cell has a ~23°C difference between the smallest and the largest air mass flow rates. In order to quatify how these systems responded to the air mass flow rate change, the settling time for each temperature variation is given in Table 7 for both systems.

Table 7 Settling times (hours) for each temperature variation described in Figures 22 and 23.

Location	1 cell			48 cells		
	1.43 $\times 10^{-5}$ g/s per BPP	2.86$\times 10^{-5}$ g/s per BPP	5.72$\times 10^{-5}$ g/s per BPP	1.43 $\times 10^{-5}$ g/s per BPP	2.86$\times 10^{-5}$ g/s per BPP	5.72$\times 10^{-5}$ g/s per BPP
EP	1.075	1.071	1.067	1.112	1.087	1.063
Middle MEA	1.018	1.014	1.011	0.673	0.650	0.628

It has been shown that the temperature of each layer in the fuel cell responds to changes in current and air mass flow rate at different speeds. In order to study the range of the system time constants, the fastest and slowest layers are studied. As it was discussed previously, the end plates have greater heat storage capacity than the other layers in the MEA, thus, their dynamics are slower than the other layers. Due to the fuel cell configuration, the dynamics of left end plate will be slightly slower than those of the right end plate. Moreover, it was observed in the previous simulations that the speed of

response of the different layers was different for both size stacks. Also, it was seen that the system also responded with different speeds based on the inputs (i.e., current and air mass flow rate). For this reason, the time constants were investigated as a function of number of cells forming the stack, current and air mass flow rate. Figure 22 illustrates the time constants for the left end plate and the middle MEA layer for a wide range of current, number of cells and air mass flow rates.
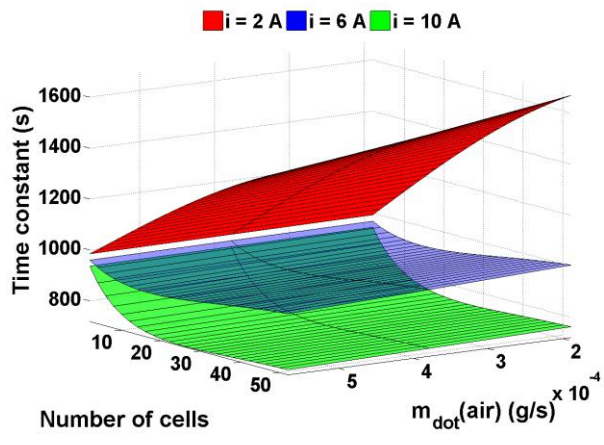
a) Left end plate

Fig. 22. Time constants for fuel cell stacks of different sizes (1 to 50 cells) and different operation conditions.
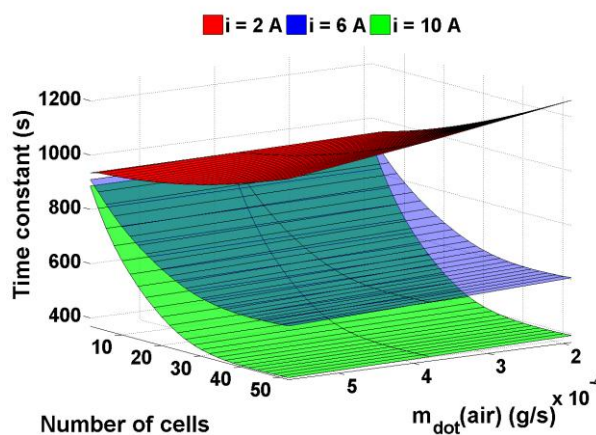
b) Middle MEA

Fig. 22. Time constants for fuel cell stacks of different sizes (1 to 50 cells) and different operation conditions. (cont)

As seen in Figure 22a, the time constants decrease as the current increase, independent of the number of cells. For 2 A, as the number of cells increases, the time constants increase. For 6 and 10 A, the behavior of the stack is opposite from what is observed at low currents: the time constants decrease as the stack size increases. However, this behavior is only true for up to 25-cell stacks. When increasing the number of cells beyond 25, the time constants again increase, even for larger currents. For 10 A, increasing the number of cells from 13 to 25, decreases the time constant of the left end plate layer by 3.3%. Increasing the number of cells even further, i.e. from 25 to 50 cells, increases the time constant by 2.4%. On the other hand, for a current of 2 A, increasing the number of cells from 13 cells to 49 cells increases the time constant by 37.8%. As observed in Figure 22b, similar to the behavior in the left end plate, as more cells are added to the stack the time constant of the middle layer decreases with increasing current.

Comparing Figures 22a and b, it is observed that at 2 A the temperature dynamics for the middle layer are only 5% faster than those of the left end plate for a single cell. However, for the same stack configuration, at 10 A the middle layer temperature

dynamics has a time constant 50% faster than those of the left end plate. Doing the same comparison for a 50-cell stack, at 2 A the middle layer temperature dynamics are 25% faster than those of the left end plate. However, at 10 A the middle layer temperature response is 51% faster than that of the left MEA. This analysis illustrates that, independent from the number of cells forming the stack, as currents increases, the time constants decrease. This explains why fuel cells are so easily scalable, making them suitable for multiple applications from power plants to portable devices.

Comparing both dynamic simulations, it can be observed that the system temperature is more sensitive to changes in current than it is to changes in air mass flow rate. This behavior is supported by the time constant plots where the maximum change in the time constants due to the effects of air mass flow rate is a 13.7% increase for the middle MEA in a 51-cell stack operating at 2 A. Therefore, it can be concluded that for thermal management purposes, the operating current will have a greater influence on the stack temperature than the air mass flow rate.

The fuel cell system dynamics can be explained by isolating the MEA dynamics. Rearranging the term a_{33} described by equation (71) and introducing the simplifications mentioned in the previous section yields

$$a_{33} = -h_{chan}A_{MEA}^{V}\left(\frac{2\dot{m}_{air}c_{air}+h_{chan}A_{MEA}^{V}}{2\dot{m}_{air}c_{air}+h_{chan}\left(A_{BPP}^{V}+A_{MEA}^{V}\right)}\right) - \frac{A_{BPP}^{L}}{R_{BPP,MEA}^{"}} - \frac{A_{BPP}^{S}}{R_{BPP,MEA}^{"}} + iA_{MEA}\left(\frac{\Delta s}{2F}\right)(106)$$

Note that since the entropy term in equation (106) is negative for the fuel cell reaction, a_{33} will remain negative for all air mass flow rates and all currents. As the air mass flow rate tends to zero,

$$\frac{2\dot{m}_{air}c_{air}+h_{chan}A_{MEA}^{V}}{2\dot{m}_{air}c_{air}+h_{chan}\left(A_{BPP}^{V}+A_{MEA}^{V}\right)} \to \frac{A_{MEA}^{V}}{\left(A_{BPP}^{V}+A_{MEA}^{V}\right)} \tag{107}$$

On the other hand, as the air mass flow rate tends to infinity,

$$\frac{2\dot{m}_{air}c_{air}+h_{chan}A_{MEA}^{V}}{2\dot{m}_{air}c_{air}+h_{chan}\left(A_{BPP}^{V}+A_{MEA}^{V}\right)} \to 1 \tag{108}$$

Therefore, this term is bounded between 0.162 and 1. Also, it can be seen that the current dependent term in a_{33} is not upper bounded and tends to zero as the current tends to zero. Since this term is negative, as current tends to infinity, the term will tend to $-\infty$. The time constant describing the MEA dynamics is approximately

$$t_c^{MEA} = \frac{\tau_{MEA}}{a_{33}} \qquad (109)$$

Since the MEA thermal mass is fixed for each layer, as a_{33} increases, the time constant decreases. As the previous discussion shows, a_{33} is more sensitive to changes in current than it is to changes in mas flow rate (since this term is upper and lower bounded). This analysis mathematically explains the observations previously noted for Figure 22. Furthermore, the electrical power generated in the fuel cell is directly proportional to the number of cells in the stack. As the number of cells increases, the electrical power generated by the stack increases accordingly, as does the heat generated. Since the electric power generated by a PEM fuel cell is approximately the same as the heat produced [28], as more current is demanded from the fuel cell, the more heat is generated and hence, the smaller the time constants are. The current affects some coefficients in the **A** matrix (a_{33} and the subsequent repeating terms as the number of cells is increased) and affects the time constants accordingly, i.e., as current is increased, the time constants decrease.

In order to analyze the fuel cell temperature response as a function of number of cells it will be assumed that the stack is only formed by MEA layers since these are the only layers in the stack generating heat. In this case, **A**$_{ss}$ can be approximated to a diagonal matrix formed by a_{33} terms, and the time constants would be equal to the thermal mass matrix multiplied by the inverse of **A**$_{ss}$. Computing the determinants of the two multiplying matrices yields

$$t_c \approx \frac{\tau^n}{\left(a_{33}^c + a_{33}^i i\right)^n} \qquad (110)$$

where n is the number of cells, a_{33}^c is the terms of a_{33} that are not dependent on current and a_{33}^i is the term of a_{33} that is dependent on current. The current-dependent term in a_{33} is three orders of magnitude smaller than a_{33}^c. Therefore,

$$t_c \approx \frac{\tau^n}{\left(a_{33}^c + a_{33}^i i\right)^n} \approx \frac{\tau^n}{\left(a_{33}^c\right)^n} \tag{111}$$

Since a_{33}^c is constant, as more layers are added to the system, the larger becomes the thermal mass and the greater becomes the system time constant. This trend is what Figure 22 showed since even for high current, the time constants increased for large number of cells.

6 Summary and Conclusions.

This paper presented an analytical one-dimensional lumped model for an open cathode polymer electrolyte fuel cell. Studying the errors resulting from neglecting different terms in the model, it can be concluded that the changes in enthalpies and the heat generated in the bipolar plates can be ignored since neglecting these terms only leads to simulation errors less than 1%. However, despite the fact that the term including the air mass flow rate in the convection energy balance is negligible compared to the other terms, ignoring this term yields simulation errors up to 28.4%. Also, neglecting these terms creates a solution where layer temperatures increase as air mass flow rate increases. Therefore, this solution not only gives a high numerical error, it also gives a steady state solution that does not make physical sense. Moreover, since the heat generation in the bipolar plates is insignificant and can be neglected, only the heat generated in the MEA dictates the heat generation in the fuel cell.

In order to validate the model presented and its steady state analysis, an analogy between the fuel cell and a heat exchanger was made and validated. The heat exchanger analysis brings new insight to the study of fuel cells as an adiabatic steady state fuel cell thermal model. A new reverse engineering perspective is given for the design of fuel cells: the heat generated in the fuel cell can be determined first given a desired operating

temperature. Knowing the heat generation in the fuel cell, the voltage losses, which determine the specific characteristics of the desired fuel cell, can be calculated.

Moreover, in order to study the dynamic behavior of the temperatures in the fuel cell as air mass flow rate, current and number of cells vary, two dynamic simulations were conducted. It has been shown that the number of cells, the current drawn and the mass flow rate of air circulating through the stack affect the system time constants. The heat generated by the fuel cell is affected by the number of cells that form the stack. On the other hand, the larger the stack, the greater the overall system thermal mass. Therefore, increasing the number of cells also increases the amount of heat energy that can be stored in the stack. This ratio between heat storage and heat generation determines the system time constant as well as the steady state temperatures for all of the layers. Finally, this paper illustrates how the fuel cell temperature response changes with different inputs, i.e., air mass flow rate and operating current. It has been shown that the fuel cell steady-state and dynamic temperature is more sensitive to changes in current than to changes in air mass flow rate for any stack size. Furthermore, it has been shown that increasing the air mass flow rate of the current, yields a decrease in the system time constant. Finally, it was presented that since the current-dependent term in $\mathbf{A_{ss}}$ is negligible compared to the other terms multiplying the MEA temperature, as the system thermal mass is increased by adding more cells to the stack, the time constants are also increased.

References

[1]   J. Amphlett, R. Baumert, R. Mann, B. Peppley and P. Roberge, *Performance modeling of the ballard mark IV solid polymer electrolyte fuel cell*, J. of Electrochemical Soc., 1995: 142(1):5.

[2]   J. Amphlett, R. Mann, B. Peppley, P. Roberge and A. Rodrigues, *A model predicting transient responses of proton exchange membrane fuel cells*, J. of Power Sources, 1996:61:6.

[3]   M. Wöhr, K. Bolwin, W. Schnurnberger, M. Fischer, W. Neubrand and G. Eigenberger, *Dynamic modeling and simulation of a polymer membrane fuel cell including mass transport limitation*, Int. J. of Hydrogen Energy, 1998:23(3):6.

[4]   J.H. Lee and T.R. Lalk, *Modeling fuel cell stack system*, J. of Power Sources, 1998: 73: 229-241.

[5]   R.F. Mann, J.C. Amphlett, M.A. Hooper, H.M. Jensen, B.A. Peppley and P.R. Roberge, *Development and application of a generalized steady-state electrochemical model for a PEM fuel cell*, Int. J. of Power Sources, 2000:86:8.

[6]   N. Djilali and D. Lu, *Influence of heat transfer on gas and water transport in fuel cells*, Int. J. of Thermal Sciences, 2000:41:29-40.

[7]   L. Wang, A. Husar, T. Zhou and H. Liu, *A parametric study of PEM fuel cell performances*, Int. J. of Hydrogen Energy, 2003:28:1263-72.

[8]   W. Yan, F. Chen, H. Wu, C. Soong and H. Chu, *Analysis of thermal and water management with temperature-dependent diffusion effects in membrane of proton exchange membrane fuel cells*, J. of Power Sources, 2004:129:11.

[9]   X. Xue, J. Tang, A. Smirnova, R. England and N. Sammes, *System level lumped-parameter dynamic modeling of PEM fuel cell*, J. of Power Sources, 2004:133(17):188-204.

[10]   H. Ju, H. Meng and C.Y. Wang, *A single-phase, non-isothermal model for PEM fuel cells*, Int. J. of Heat and Mass Transfer, 2005:48:1303-1315.

[11]   Y. Shan and S. Choe, *Modeling and simulation of a PEM fuel cell stack considering temperature effects*, J. of Power Sources, 2006:158(13): 274-286.

[12]   C. Bao, M. Ouyang and B. Yi, *Modeling and control of air stream and hydrogen flow with recirculation in a PEM fuel cell system – I. Control-oriented modeling*, Int. J. of Hydrogen Energy, 2006:31:1879-96.

[13]   M.U. Iftikhar, D. Riu, F. Druart, S. Rosini, Y. Bultel and N. Retière, *Dynamic modeling of proton exchange membrane fuel cell using non-integer derivatives*, J. of Power Sources, 2006:160:1170-1182.

[14]   B. Blunier and A. Miraoui, *Modelling of fuel cells using multi-domain VHDL-AMS language*, J. of Power Sources, 2007:177(2):434-450.

[15]   Y-T. Lin, C-T. Lin, Y-C. Chen, K-M. Yin and C-T. Yang, *An analytical study of the PEM fuel cell with axial convection in the gas channel*, Int. J. of Hydrogen Energy, 2007:32:4477-4488.

[16]   A.J. del Real, A. Arce and C. Bordons, *Development and experimental validation of a PEM fuel cell dynamic model*, J. of Power Sources, 2007:173(1):310-324.

[17]   C. Spiegel, *Mathematical modeling of polymer exchange membrane fuel cells*, University of Florida, Graduate School Theses and Dissertations, 2008:Paper 510

[18]   F. Gao and B. Blunier, *Cell layer generalized dynamic modeling of a PEMFC stack using VHDL-AMS language,* Int. J. of Hydrogen Energy, 2009:34:5498-5521.

[19]   B.P.M. Rajani and A.K. Kolar, *A model for a vertical planar air breathing PEM fuel cell*, J. of Power Sources, 2007:164:210-221.

[20]   A.P. Sasmito, K.W. Lum, E. Birgersson and A.S. Mujumdar, *Computational study of forced air-convection in open-cathode polymer electrolyte fuel cell stacks*, J. of Power Sources, 2010:195:5550-5563.

[21]   R. O'Hayre, T. Fabian, S. Lister, F.B. Prinz and J.G. Santiago, *Engineering model of a passive planar air breathing fuel cell cathode*, J. of Power Sources, 2007:167:118-129.

[22]   S.O. Morner and S.A. Klein, *Experimental evaluation of the dynamic behavior of an air-breathing fuel cell stack*, J. of Solar Energy Engineering, 2001:123:225-231.

[23]   S. Lister and N. Djilali, *Theoretical performance analysis of microstructured air-breathing fuel cells*, Electrochem. and Solid-State Letters, 2008:11:B1-B5.

[24]   F.P. Incropera, D.P. DeWitt, T.L. Bergman and A.S. Lavine, *Fundamentals of heat and mass transfer*, (4th ed.), New York, John Wiley and Sons, Inc.,1996.

[25]   C. Spiegel, *PEM fuel cell modeling and simulation using Matlab*, Amsterdam, Academic Press/Elsevier, 2008.

[26]   F. Barbir, *PEM fuel cells: theory and practice*, Amsterdam, Academic Press/Elsevier, 2005.

[27]   J. Kim, S.M. Lee and S. Srinivasan, *Modeling of proton exchange membrane fuel cell performance with an empirical equation*, J. of Electrochemical Society, 1995:142(8):2670-2674.

[28]   H. Ju, H. Meng and C.H. Wang, *A single-phase, non-isothermal model for PEM fuel cells*, Int. J. of Heat and Mass Transfer, 2005:48:1303-1315.

[29]   R. O'Hare, S.W. Cha, W. Colella and F.B. Prinz, *Fuel cell fundamentals*, New York, John Wiley and Sons, Inc., 2009.

[30]   T.E. Springer, T.A. Zawodzinski and S. Gottesfeld, *Polymer electrolyte fuel cell model*, J. of the Electrochemical Society, 1991:138(8):2334-2342.

[31]   S-K. Park and S-Y. Choe, *Dynamic modeling and analysis of a 20-cell PEM fuel cell stack considering temperature and two-phase effects*, J. of Power Sources, 2008:179:660-672.

[32]   M. Khandelwal and M.M. Mench, *Direct measurement of through-plane thermal conductivity and contact resistance in fuel cell materials*, J. of Power Sources, 2006:161:1106-1115.

[33]   J. Kennedy and R. Eberhart, *Particle swarm optimization*, IEEE International Conference on Neural Networks, 1995:1942-1948.

SECTION

3. SUMMARY, CONCLUSIONS AND FUTURE WORK

This thesis presents a one-dimensional lumped model for an open cathode polymer electrolyte fuel cell. Studying the errors resulting from neglecting different terms in the model, it can be concluded that the changes in enthalpies and the heat generated in the bipolar plates can be ignored since neglecting these terms only leads to simulation errors less than 1%. However, despite the fact that the term including the air mass flow rate in the convection energy balance is negligible compared to the other terms, ignoring this term yields simulation up to 28.4%. Also, neglecting these terms creates a solution where layer temperatures increase as air mass flow rate increases. Therefore, this solution not only gives a high numerical error, it also gives a steady state solution that does not make physical sense. Moreover, since the heat generation in the bipolar plates is insignificant and can be neglected, only the heat generated in the MEA dictates the heat generation in the fuel cell.

In order to validate the model presented and its steady state analysis, an analogy between the fuel cell and a heat exchanger is made. The heat exchanger analysis brings new insight to the study of fuel cells as an adiabatic steady state fuel cell thermal model. A new reverse engineering perspective is given for the design of fuel cells: the heat generated in the fuel cell can be determined first given a desired operating temperature. Knowing the heat generation in the fuel cell, the voltage losses, which determine the specific characteristics of the desired fuel cell, can be calculated.

Moreover, in order to study the dynamic behavior of the temperatures in the fuel cell as air mass flow rate, current and number of cells are varied, two dynamic simulations were analyzed varying these parameters. It has been shown that the number of cells, the current drawn and the mass flow rate of air circulating through the stack affect the system time constants. The heat generated by the fuel cell is affected by the number of cells that form the stack. On the other hand, the larger the stack, the greater

the overall system thermal mass. Therefore, increasing the number of cells also increases the amount of heat energy that can be stored in the stack. This ratio between heat storage and heat generation determines the system time constant as well as the steady state temperatures for all of the layers. Finally, this paper illustrates how the fuel cell temperature response changes with different inputs, i.e., air mass flow rate and operating current. It has been shown that the fuel cell temperature is more sensitive to changes in current does to changes in air mass flow rate for any stack size.

This thesis is directed toward control oriented modeling. In order to get there, the model presented would have to be linearized and reduced. Once the model is reduced to a manageable number of states, the dynamics described fully supports the design of a controller.

APPENDIX A

AIR MASS FLOW RATE OBTAINED THROUGH FAN OPERATION

In order to determine the air mass flow rate through each channel, the pressure drop across the channels is calculated

$$\Delta p = f \frac{\rho \left(\dot{m}_{air} / \rho A_{chan} \right)^2}{2D_H} w_{BPP} \tag{1}$$

where A_{chan} is the channel cross sectional area (m^2). The air moving through the channels in the bipolar plates is driven by two fans that pull air through them. In order to determine the system operating condition, the fan's characteristic curve is compared to the system's characteristic curve. The intersection between the characteristic curve of the fan and equation (3) determines the fuel cell operating point i.e., set point. Using the fan laws and knowing a set point, it is possible to calculate the fan performance at a second condition, and the air mass flow rate in the channels can be calculated. Since the fans are placed in parallel, i.e. side by side, the pressure drop across them will be the same. However, the amount of air they can move together doubles the amount of air that a single fan can move. Bearing this in mind and calculating the pressure drop across the fuel cell with equation (3), the system operation set point is illustrated in Figure 4.1.
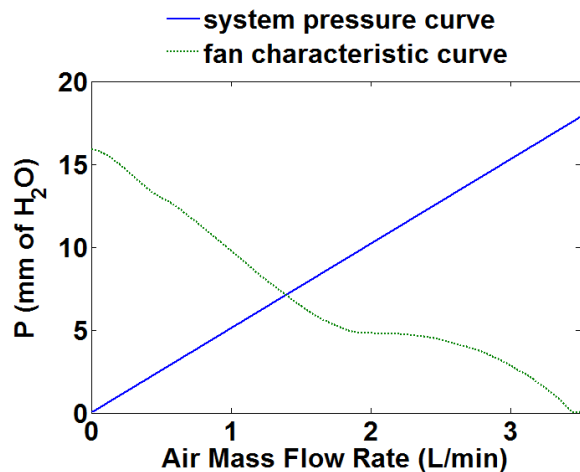

Figure 1A. Fuel cell – fan operation point.

Figure 4.1 showed the characteristic curve for one fan operating at a constant 12VDC (dotted line), i.e., maximum speed. As seen in Figure 4.1 the air mass flow rate provided by the fan setup at their maximum speed with the fuel cell acting as a resistance to the flow is 1.39L/min.   This air mass flow rate is the one used throughout the model described in this research.

APPENDIX B

MODEL UNCERTAINTIES

The parameters obtained through the Particle Swarm Optimization (PSO) are unknown parameters in every fuel cell. In order to study the model robustness, the uncertainty of each of the parameters found in equation (88) was determined. The uncertainty of each parameter can be found in Table 1B.

Parameter	PSO Value	Uncertainty ($\pm$%)
A_{act}	14.22	40
R	0.6817	20
A	0.01	99
m	0.612	10
n	0.7099	40

TABLE 1B Parameter uncertainty.

Varying the parameters within these bounds yields to deviations of up to 3% in the steady state temperatures.

BIBLIOGRAPHY

[1]   *Kyoto protocol to theUnited Nations framework convention on climate change,*
        United Nations, http://unfccc.int/kyoto_protocol/items/2830.php (date last
        accessed May 30th 2012)

[2]   EG&G Technical Services, Inc., Science Applications International Corporation.
        Fuel Cell Handbook. (2002) ed. 6.

[3]   R. O'Hare, S. W. Cha, W. Colella, F. B. Prinz, Fuel cell fundamentals, New York.
        John Wiley AND Sons, Inc., 2009.

[4]   J. Amphlett, R. Baumert, R. Mann, B. Peppley and P. Roberge, *Performance
        modeling of the ballard mark IV solid polymer electrolyte fuel cell*, J. of
        Electrochemical Soc., 1995: 142(1):5.

[5]   J. Amphlett, R. Mann, B. Peppley, P. Roberge and A. Rodrigues, *A model
        predicting transient responses of proton exchange membrane fuel cells*, J. of
        Power Sources, 1996;61:6.

[6]   M. Wöhr, K. Bolwin, W. Schnurnberger, M. Fischer, W. Neubrand and G.
        Eigenberger, *Dynamic modeling and simulation of a polymer membrane fuel cell
        including mass transport limitation*, Int. J. of Hydrogen Energy, 1998;23(3):6.

[7]   J.H. Lee and T.R. Lalk, *Modeling fuel cell stack system,* J. of Power Sources,
        1998: 73: 229-241.

[8]   R.F. Mann, J.C. Amphlett, M.A. Hooper, H.M. Jensen, B.A. Peppley and P.R.
        Roberge, *Development and application of a generalized steady-state
        electrochemical model for a PEM fuel cell,* Int. J. of Power Sources, 2000;86:8.

[9]   N. Djilali and D. Lu, *Influence of heat transfer on gas and water transport in fuel
        cells,* Int. J. of Thermal Sciences, 2000;41:12.

[10]   L. Wang, A. Husar, T. Zhou and H. Liu, *A parametric study of PEM fuel cell
        performances,* Int. J. of Hydrogen Energy. 2003;28:1263-72.

[11]   W. Yan, F. Chen, H. Wu, C. Soong and H. Chu, *Analysis of thermal and water
        management with temperature-dependent diffusion effects in membrane of proton
        exchange membrane fuel cells,* J. of Power Sources., 2004;129:11.

[12]   X. Xue, J. Tang, A. Smirnova, R. England and N. Sammes, *System level lumped-
        parameter dynamic modeling of PEM fuel cell,* J. of Power Sources,
        2004:133(17): 188-204.

[13]   H. Ju, H. Meng and C.Y. Wang, *A single-phase, non-isothermal model for PEM fuel cells,* Int. J. of Heat and Mass Transfer, 2005: 48: 1303-1315.

[14]   Y. Shan and S. Choe, *Modeling and simulation of a PEM fuel cell stack considering temperature effects,* J. of Power Sources, 2006:158; 13 274-286.

[15]   C. Bao, M. Ouyang and B. Yi, *Modeling and control of air stream and hydrogen flow with recirculation in a PEM fuel cell system – I. Control-oriented modeling,* Int. J. of Hydrogen Energy, 2006:31;1879-96.

[16]   M.U. Iftikhar, D. Riu, F. Druart, S. Rosini, Y. Bultel and N. Retière, *Dynamic modeling of proton exchange membrane fuel cell using non-integer derivatives*, J. of Power Sources, 2006: 160; 1170-1182.

[17]   B. Blunier and A. Miraoui, *Modelling of fuel cells using multi-domain VHDL-AMS language,* J. of Power Sources, 2007: 177 (2); 434-450.

[18]   Y-T. Lin, C-T. Lin, Y-C. Chen, K-M. Yin and C-T. Yang, *An analytical study of the PEM fuel cell with axial convection in the gas channel,* Int. J. of Hydrogen Energy, 2007;32:4477-4488.

[19]   A.J. del Real, A. Arce and C. Bordons, *Development and experimental validation of a PEM fuel cell dynamic model,* J. of Power Sources, 2007:173 (1); 310-324.

[20]   C. Spiegel, *Mathematical modeling of polymer exchange membrane fuel cells.*

[21]   F. Gao and B. Blunier, *Cell layer generalized dynamic modeling of a PEMFC stack using VHDL-AMS language,* Int. J. of Hydrogen Energy, 2009: 34; 5498-5521.

[22]   B.P.M Rajani and A.K. Kolar, *A model for a vertical planar air breathing PEM fuel cell*, J. of Power Sources, 2007: 164; 210-221.

[23]   A.P.Sasmito, K.W. Lum, E. Birgersson and A.S.Mujumdar, *Computational study of forced air-convection in open-cathode polymer electrolyte fuel cell stacks*, J. of Power Sources, 2010: 195; 5550-5563.

[24]   R. O'Hayre, T. Fabian, S. Lister, F.B. Prinz and J.G. Santiago, *Engineering model of a passive planar air breathing fuel cell cathode*, J. of Power Sources, 2007: 167; 118-129.

[25]   S.O. Morner and S.A. Klein, *Experimental evaluation of the dynamic behavior of an air-breathing fuel cell stack*, J. of Solar Energy Engineering, 2001: 123; 225-231.

[26]   S. Lister and N. Djilali, *Theoretical performance analysis of microstructured air-breathing fuel cells*, Electrochem. and Solid-State Letters, 2008: 11; B1-B5.

VITA

Blanca Ollero Loranca was born in Madrid, Spain. In May 2010, she received her B.S. in Mechanical Engineering from Saint Louis University, St. Louis, Missouri. In August 2012, she received her M.S. in Mechanical Engineering from Missouri University of Science and Technology, Rolla, Missouri.